Linear gyrokinetic theory for kinetic magnetohydrodynamic eigenmodes in tokamak plasmas

H. Qin, W. M. Tang, and G. Rewoldt
Princeton Plasma Physics Laboratory, Princeton University, Princeton, New Jersey 08543

(Received 15 January 1999; accepted 17 March 1999)

A two-dimensional (2D) numerical solution method is developed for the recently derived linear gyrokinetic system which describes arbitrary wavelength electromagnetic perturbations in tokamak plasmas. The system consists of the gyrokinetic equation, the gyrokinetic Poisson equation, and the gyrokinetic moment equation. Since familiar magnetohydrodynamic (MHD) results can be recovered entirely from this gyrokinetic model, and all interesting kinetic effects are intrinsically included, this gyrokinetic system offers an approach for kinetic MHD phenomena which is more rigorous, self-consistent, and comprehensive than the previous hybrid models. Meanwhile, drift type microinstabilities can be also investigated systematically in this theoretical framework. The linear gyrokinetic equation is solved for the distribution function in terms of the perturbed fields by integrating along unperturbed particle orbits. The solution is substituted back into the gyrokinetic moment equation and the gyrokinetic Poisson equation. When the boundary conditions are incorporated, an eigenvalue problem is formed. The resulting numerical code, KIN-2DEM, is applied to kinetic ballooning modes, internal kink modes, and toroidal Alfvén eigenmodes (TAEs). The numerical results are benchmarked against the well-established FULL code [G. Rewoldt, W. M. Tang, and M. S. Chance, Phys. Fluids **25**, 480 (1982)], the PEST code [J. Manickam, Nucl. Fusion **24**, 595 (1984)], and the NOVA-K code [C. Z. Cheng, Phys. Rep. **211**, No. 1 (1992)]. More importantly, kinetic effects on MHD modes can be investigated nonperturbatively. In particular, the kinetic effects of the background plasma on internal kink modes and the hot particle destabilization of TAEs are studied numerically. © *1999 American Institute of Physics.*
[S1070-664X(99)03806-9]

I. INTRODUCTION

Recent experimental and theoretical studies have demonstrated that a kinetic description for electromagnetic modes in tokamak plasmas is important for the understanding of electromagnetic drift waves and kinetic-magnetohydrodynamic (MHD) phenomena. Finite β effects for the electrostatic drift wave were first addressed by Rosenbluth and Sloan.[1] Tang[2] pointed out three physical mechanisms due to the finite plasma β that are important: the diamagnetic or ''self-dug'' well generated by plasma pressure, the Shafranov shift of flux surfaces, and the coupling between drift waves and shear Alfvén waves. While the diamagnetic well and the Shafranov shift are equilibrium effects which can be incorporated by using realistic MHD equilibrium solutions, the coupling between drift waves and Alfvén waves is a dynamic effect. To investigate this coupling, we have to use an electromagnetic equation system. The finite β effect on drift modes is generally found to be stabilizing. For example, examination of electromagnetic η_i modes in slab geometry[3] and in toroidal geometry[4,5] revealed that increasing plasma β can provide a stabilizing effect, especially when finite Larmor radius (FLR) effects for ions become important.

As tokamaks approach ignition conditions, the physical effects due to energetic particles become more and more prominent. It has been discovered in the past two decades that the interplay between the kinetic effects described by the Vlasov–Maxwell system and the fluid modes determined by the MHD model produces a new breed of instabilities—kinetic MHD modes. The fishbone mode is probably the first kinetic MHD mode observed in tokamak plasmas.[6] The observed fishbone bursts are strongly correlated with losses of injected energetic beam ions. The study of fishbone modes is of practical interest because the losses of energetic beam ions reduce the plasma β significantly. Experimental evidence also showed the dominant mode structure to be a $(m,n)=(1,1)$ mode. Chen *et al.*[7] first used a kinetic MHD model to explain theoretically the fishbone oscillations. It was found that trapped energetic particles can destabilize the internal kink mode.

Another well-known example of kinetic MHD modes is the toroidal Alfvén eigenmode (TAE).[8] TAEs can be destabilized by alpha particles and other energetic particles when the pressure of energetic particles is high enough.[9,10] This conclusion could have serious implications for ignited fusion reactors. Unstable TAE modes, driven by energetic particles, can induce significant energetic particle losses which may in turn reduce plasma β and damage the reactor wall. Both experimental and theoretical studies confirmed that TAE modes can lead to 80% of the energetic particle transport in present tokamaks.[11]

The well-studied kinetic ballooning mode (KBM) also falls into the category of kinetic MHD modes. Kinetic ballooning mode theory in general geometry was introduced by Tang *et al.*[12] and Frieman *et al.*[13] as a systematic procedure for studying the influence of kinetic effects on the stability of MHD ballooning modes. A numerical analysis for the kinetic ballooning mode was performed by Rewoldt *et al.*[4] The ki-

netic ballooning modes can be driven unstable by kinetic effects such as trapped particles and temperature gradients when the plasma β is above some critical value. Therefore, study of kinetic ballooning modes is important in understanding the plasma β limit imposed by it.

The interaction between energetic particles and sawtooth crashes is also a current topic in kinetic MHD theory. The sawtooth instability can often result in major disruptions which terminate plasma discharges. It limits the current density on the magnetic axis and produces large-scale transport in the core plasma. Recent experiments in Joint European Torus (JET) discovered that energetic particles heated by Ion Cyclotron Resonance Frequency (ICRF) waves have a strong stabilizing effect on the resistive internal kink mode.[14] The JET results were confirmed numerically by White *et al.*, using a kinetic MHD simulation. [15]

The current methods used for kinetic MHD instabilities are mostly hybrid ones,[7,10,16,17] and are generally perturbative extensions to MHD models. There, energetic particles are assumed to have a much smaller β than the bulk plasma. Energetic particles interact with the bulk plasma through the ∇P term in the MHD equation, that is, replacing ∇P by $\nabla(P+P_h)$, where P_h is the pressure of ''hot'' particles which is solved for from the gyrokinetic equation or the drift kinetic equation in terms of the perturbed electromagnetic field. In many applications, the coupled equation system is not solved self-consistently.[10,18–20] Especially in analytical calculations,[7] eigenfrequencies are often not calculated self-consistently from the eigenequations, but rather are estimates from a kinetically modified version of the usual MHD energy integral. Moreover, kinetic effects are usually assumed to be small and the mode structures are assumed to be no different than those of the corresponding pure MHD modes. Only the eigenfrequencies are perturbed. A standard hybrid kinetic MHD model is dominantly a MHD model with small kinetic perturbations. Different kinetic MHD models differ in how the MHD system is kinetically perturbed. The mathematical validity of such approaches cannot be justified rigorously, even though the physics insight is very productive.

Hybrid models have some serious limitations, all of which are related to the basic assumption that kinetic effects are small perturbations for the MHD modes. Since kinetic effects enter only through the ∇P term in the MHD equations, the basic characteristics of the MHD model are unchanged. With the introduction and increased use of high power auxiliary heating techniques such as neutral beam injection and ion cyclotron resonant heating, modern tokamaks contain large number of energetic particles. Inevitably, future ignited fusion reactors will involve many more energetic particles. It is generally agreed that these energetic particles cannot be described by the MHD model. The large number of energetic particles and their strong interaction with the bulk plasma may prohibit the use of the MHD description even for the bulk plasmas.

The restrictions of the MHD model include the lack of kinetic resonances and the inaccuracy in its description of parallel dynamics. Kinetic resonances, such as Landau damping, are obviously important. For the fluid model to be valid, there must be some kind of force to ''glue'' particles together so that a group of nearby particles can be treated as a fluid element. In a collisionless plasma, the Lorentz force acts as such a ''glue'' in the perpendicular directions. However, in the parallel direction, the particles are almost free-streaming. A fluid model is not valid in the parallel direction. This inaccuracy in the MHD model is partially manifested in the fact that, for MHD modes, $E_{\|}=0$. As we know, parallel dynamics are controlled by kinetic resonances and parallel accelerations. Since kinetic resonances are not included in a standard fluid model, the parallel acceleration must vanish. This results in an infinite conductivity in the parallel direction when there are no Coulomb collisions.

All these shortcomings associated with the standard fluid model can be readily overcome by the Vlasov–Maxwell system. A fully kinetic model naturally picks up all the kinetic effects. But in order to address the kinetic MHD problems, the kinetic system must be an electromagnetic system which includes the kinetic equation and all of the Maxwell equations. This could complicate the problem significantly, especially in general geometry. This kind of complication is expected because the full Vlasov–Maxwell system essentially covers almost all the interesting problems in tokamak plasmas. The more general the model, the less tractable it is.

Substantial progress in this area has been made since the 1980s. An electromagnetic gyrokinetic equation was derived by Catto *et al.*,[21] and Antonsen *et al.*[22] Gyrokinetic theory takes advantage of the fact that, in a strongly magnetized plasma, particles' gyroradii are much smaller than the scale length of the total magnetic field. The fast time scale gyromotion is averaged out from the system. (New developments of gyrokinetic perpendicular dynamics which extend the gyrokinetic model to compressional Alfvén modes and arbitrary frequency modes are reported in Ref. 23.) In the meantime, a fully kinetic model and a comprehensive numerical code for high-n kinetic ballooning modes were developed.[4,12,13,24] It represented the first fully kinetic model for low frequency electromagnetic instabilities. It was shown to be reducible to the MHD ballooning equation in some reasonable limits. MHD results can be recovered completely from the kinetic side. On the other hand, kinetic effects due to trapped particles, temperature gradients, and Landau damping were fully retained. The kinetic MHD phenomena in these modes were studied without using the MHD equations.

The kinetic ballooning model circumvents the geometry problem by looking at only high mode number ballooning modes. Because the mode wavelength is much shorter than the equilibrium scale length, some background variations are not important at all. This is not true for low mode number global modes, the study of which requires us to consider all possible background variations. Previous gyrokinetic equations were mainly derived for the high mode number (i.e., short wavelength) modes,[21,22,25–35] for which some of the background inhomogeneities are not important and are left out. However, the most crucial physical factors driving the long wavelength modes, such as the toroidal Alfvén eigenmode[8,9] and the internal kink mode,[36–38] are the background inhomogeneities which include the inhomogeneities of the magnetic field, temperature, and density. Part of the

inhomogeneity of the magnetic field enters through the current distribution. For this purpose, we have to reexamine the basic gyrokinetic equation system as well. For the electromagnetic drift waves, a comprehensive gyrokinetic system which can fully recover the MHD modes is needed to study the interaction between drift modes and Alfvén waves. Such a system only exists for high mode number ballooning modes.[4,24]

Furthermore, in magnetized plasmas there exist a lot of multi-scale-length modes. Actually, the well-known internal kink mode is indeed a multi-scale-length mode. For an unstable internal kink mode, there is a boundary layer around the rational surface, inside which the scale length is much shorter than that outside. FLR effects are important inside the boundary layer, whereas, outside the boundary layer, it is just a long wavelength MHD mode. Obviously this structure cannot be described by the conventional approaches, neither the long wavelength ideal MHD theory nor the short wavelength kinetic theory. An arbitrary wavelength kinetic approach will provide us with a tool for this kind of multi-scale-length structure.

Recently, we derived a linear gyrokinetic system for arbitrary wavelength electromagnetic perturbations using the phase space Lagrangian Lie perturbation method which allows us to treat the background variations and kinetic effects rigorously.[39,40] The system consists of the gyrokinetic equation, the gyrokinetic Poisson equation, and the gyrokinetic moment equation. Background variations are fully retained in this model, and therefore the usual MHD model can be recovered from the gyrokinetic system when the kinetic effects are neglected. Since familiar MHD modes can be recovered entirely from the kinetic side, and all kinetic effects are intrinsically included, this gyrokinetic system offers an approach for kinetic MHD phenomena which is more rigorous, self-consistent, and comprehensive than the previous hybrid models. Meanwhile, drift type microinstabilities and their associated transport can also be investigated systematically in this theoretical framework. This gyrokinetic system is an arbitrary wavelength approach. It can be used to study high mode number modes, global modes (low mode number modes), and intermediate mode number modes. It is therefore suitable for those multi-scale-length structures. Not only do we recover the existing results such as the electrostatic limit,[41,42] the long wavelength limit,[43] and the ballooning limit, but also we can explore many new problems, for example, the intermediate wavelength regime and the coupling between drift waves and shear Alfvén waves.

In this paper, we describe the solution method for the linear eigenvalue problem and apply it to kinetic ballooning modes, internal kink modes, and TAEs. The gyrokinetic equation is solved for the perturbed distribution function by integrating along the unperturbed orbits. Substituting this solution back into the gyrokinetic Poisson equation and the gyrokinetic moment equation yields the eigenmode equation. The eigenvalue problem is then solved by using a Fourier decomposition in the poloidal direction and a finite element method in the radial direction. A computer algebra package for symbolic vector analysis was developed as well in order to efficiently deal with the complicated vector analysis. The resulting numerical code, KIN-2DEM, has been systematically benchmarked against well-established codes in appropriate parameter regimes. In the analysis of kinetic ballooning modes in the short wavelength limit (high-n with n being the toroidal mode number), numerical results from the KIN-2DEM code are found to be in reasonable agreement with those from the well known high-n FULL code.[4] When applied to the internal kink mode, KIN-2DEM recovered MHD results. Specially, numerical results from KIN-2DEM and PEST code[44] are consistent. When kinetic effects due to trapped ions are included, it is found that they can significantly modify the growth rate (γ) versus central safety factor (q_0) curve. Toroidal Alfvén eigenmodes (TAEs) were also studied using the present gyrokinetic analysis. Both analytic and numerical results from the gyrokinetic model were found to agree very well with the MHD results. Destabilization of the TAEs by energetic particles are known to be vitally important for ignition-class plasmas. For the test case with Maxwellian energetic hydrogen ions, comparisons have accordingly been made between the results from the present nonperturbative, fully kinetic calculation using the KIN-2DEM code and those from the perturbative hybrid calculation with the NOVA-K code.[9,10] The agreement varies with hot particle thermal velocity. The discrepancy is mainly attributed to the differences in the basic models.

The paper is organized as follows. In Sec. II, the basic theoretical and numerical formalism is presented. Then, the kinetic ballooning mode is studied numerically in Sec. III. The internal kink mode and the TAE and their kinetic effects are studied in Sec. IV and Sec. V, respectively. In the last section, we summarize and discuss possible future work.

II. BASIC FORMALISM

Most of the important long wavelength electromagnetic modes in tokamak plasmas are shear Alfvén waves, that is, the parallel magnetic perturbation is much smaller than the perpendicular magnetic perturbation. Kink modes and TAEs fall into this category. The gyrokinetic system for the shear Alfvén wave,[39,40] previously derived using the phase space Lagrangian Lie perturbation method,[28–35] consists of the gyrokinetic equation, the gyrokinetic Poisson equation, and the gyrokinetic moment equation. We start from Littlejohn's guiding center phase space Lagrangian for magnetostatic equilibrium. When the time-dependent electromagnetic perturbation is introduced into the system, the phase space Lagrangian is perturbed accordingly. A symplectic gyrocenter transformation, which transfers the guiding center coordinates into the gyrocenter coordinates,[33–35] is then introduced in such a way that in the new gyrocenter coordinates, the perturbed phase space Lagrangian has the same symplectic structure as the unperturbed one. This effectively transfers the perturbation into the perturbed Hamiltonian while keeps the dynamic structure unperturbed. Consequently, the effects of electromagnetic perturbation show up in the pull-back transformation as well, which are necessary for the correct form of Maxwell's equations in the gyrocenter coordinates. The physics associated with the pull-back transformation, first discovered in the form of polarization term in the gyro-

kinetic Poisson equation by Lee,[28] plays an important role in the gyrokinetic formalism for the shear Alfvén mode. Following the detailed algebra in Refs. 39 and 40, we can derive the gyrokinetic equation as

$$\frac{\partial g}{\partial t}+(U\mathbf{b}+\mathbf{v}_d)\cdot\nabla g=\left(\frac{c\mathbf{b}}{eB}\times\nabla F_0\cdot\nabla-\frac{\partial F_0}{\partial\epsilon}\frac{\partial}{\partial t}\right)H_1, \quad (1)$$

with

$$f=g+H_1\frac{\partial F_0}{\partial\epsilon},$$

$$H_1=eJ_0\phi(\mathbf{X})-\frac{e}{c}J_0UA_\parallel(\mathbf{X})=eJ_0\phi(\mathbf{X})-\frac{eU}{i\omega}\nabla_\parallel J_0\psi_\parallel, \quad (2)$$

where g is nonadiabatic part of the distribution function, H_1 is the perturbed Hamiltonian, and F_0 is the equilibrium distribution function which is assumed to be Maxwellian. In addition, we have replaced $A_\parallel$ by another field variable $\psi_\parallel$, which is defined by

$$A_\parallel=\frac{c}{i\omega}(\nabla\psi_\parallel)_\parallel. \quad (3)$$

The gyrokinetic Poisson equation takes the form of quasineutrality condition,

$$\sum_j e\left[\int J_0 f\,d^3\mathbf{v}+\frac{e}{m}\nabla_\perp\frac{n_0}{\Omega^2}\nabla_\perp\phi+\frac{3e}{4m}\frac{v_t^2}{\Omega^2}\frac{n_0}{\Omega^2}\nabla_\perp^4\phi\right]=0. \quad (4)$$

Besides the gyrokinetic Poisson equation, we normally need the parallel Ampere's law to complete the system. Instead of using the parallel Ampere's law directly, we combine it with the zeroth moment of the gyrokinetic equation to get the gyrokinetic moment equation (GKM) and use it as the third equation in our equation system. This equation is often referred as the gyrokinetic moment equation, in spite of the fact that it is distinct from the gyrokinetic equation because Ampere's law has been utilized to derive it. Without repeating the derivation in Refs. 39, 40, we have the gyrokinetic moment equation as

$$-\frac{\partial}{\partial t}\left[\frac{c^2}{4\pi}\nabla\cdot\left(\frac{1}{V_A^2}\nabla_\perp\phi\right)\right]+\frac{c}{4\pi}(\mathbf{B}\cdot\nabla)\frac{(\nabla\times\nabla\times\mathbf{A})\cdot\mathbf{B}}{B^2}$$
$$+(\nabla A_\parallel\times\mathbf{b})\cdot\nabla\frac{j_{0\parallel}}{B}$$
$$=-\sum_j\int(e\mathbf{v}_d\cdot\nabla f)_j\,d^3v+\frac{1}{4\pi}\frac{c^2}{v_A^2}\left(\frac{3v_t^2}{4\Omega^2}\right)_i\nabla_\perp^4\frac{\partial\phi}{\partial t}$$
$$+\mathbf{B}\cdot\nabla\left[\frac{1}{B}\sum_j\left(\frac{e^2n}{mc}\frac{v_t^2}{2\Omega^2}\right)_j\nabla_\perp^2A_\parallel\right]+\mathbf{b}$$
$$\times\sum_j\nabla\left(\frac{cen_0v_t^2}{2B\Omega^2}\right)_j\cdot\nabla\nabla_\perp^2\phi, \quad (5)$$

where the $e\int\mathbf{v}_d\cdot\nabla f\,d^3v$ is evaluated in $(\mathbf{X},U,\mu,\xi)$ coordinates.[33–35,39,40] In $(\mathbf{X},\epsilon,\mu,\xi)$ coordinates, it should be replaced by $\int(\mathbf{v}_d\cdot\nabla f+\mu\mathbf{v}_d\cdot\nabla B\partial f/\partial\epsilon)d^3\mathbf{v}$, where ϵ is kinetic energy. This gyrokinetic system provides a fully kinetic description for shear Alfvén modes and drift modes. It recovers familiar MHD modes entirely from the kinetic side, and intrinsically includes all the kinetic effects, and therefore offers an approach for kinetic MHD phenomena which is more rigorous, self-consistent, and comprehensive than the previous hybrid models.

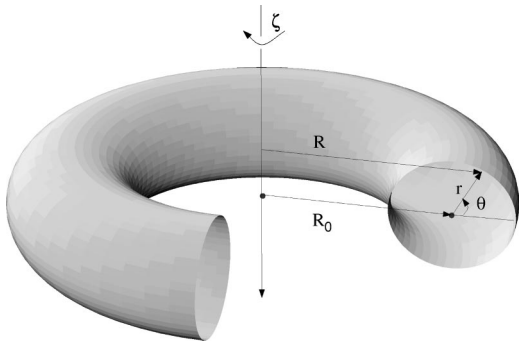

FIG. 1. Circular concentric tokamak coordinate system.

The basic solution method is to solve the linear gyrokinetic equation for the perturbed distribution function in terms of field variables, and substitute the solution back into the the quasi-neutrality condition and the gyrokinetic moment equation. When combined with boundary conditions, an eigenvalue problem is formed. The equation system is finally reduced to a coupled Ordinary Differential Equation (ODE) system in the radial direction, which is solved by a finite element method. Cubic B-spline functions are chosen as the basis functions. The eigenvalue searching algorithm by Tang and Rewoldt[43] is used. This method has been successfully applied to the kinetic theory of both short wavelength electromagnetic modes[4,24] and long wavelength electrostatic modes.[41–43,45,46] In the latter case, of course, the quasineutrality condition itself will complete the system; the gyrokinetic moment equation is not used.

We will assume the simplest tokamak geometry—a magnetic torus with circular concentric flux surfaces. The coordinates used are r, θ, and ζ, shown in Fig. 1.

The equilibrium magnetic field is given by

$$\mathbf{B}=\frac{B_0}{\alpha(\theta)}\left(\mathbf{e}_\zeta+\frac{r}{q(r)R_0}\mathbf{e}_\theta\right), \quad (6)$$

where

$$\alpha(\theta)\equiv1+\epsilon\cos\theta,\quad \epsilon\equiv\frac{r}{R_0}. \quad (7)$$

Since the toroidal direction is homogeneous, the toroidal mode number is a good quantum number for linear modes and there is no toroidal coupling. We can assume the general 2D expansion[2]

$$(\phi,\psi_\parallel)=\sum_m(\phi_m(r),\psi_{\parallel m}(r))e^{in\zeta-im\theta-i\omega t}. \quad (8)$$

We start from the gyrokinetic equation, Eq. (1). Introducing[47]

$$g=h-\left[e\frac{\partial F_0}{\partial\epsilon}-\frac{c}{i\omega B}\nabla F_0\cdot(\mathbf{b}\times\nabla)\right]J_0\psi_\parallel, \quad (9)$$

we obtain another gyrokinetic equation in terms of h, for which we will solve,

$$\frac{\partial h}{\partial t}+(U\mathbf{b}+\mathbf{v}_d)\cdot\nabla h$$
$$=\left(\frac{c\mathbf{b}}{eB}\times\nabla F_0\cdot\nabla-\frac{\partial F_0}{\partial\epsilon}\frac{\partial}{\partial t}\right)J_0\left[\phi-\left(1-\frac{\omega_d}{\omega}\right)\psi_\parallel\right], \quad (10)$$

where

$$\omega_d\equiv\frac{1}{i}\mathbf{v}_d\cdot\nabla. \quad (11)$$

We adopt the method used by Marchand *et al.*[41,42] to integrate the electromagnetic gyrokinetic equation along unperturbed orbits. The original method of Marchand *et al.* was applied to electrostatic perturbations. Here, extra effort is needed to include the shear Alfvén component.

Expanding $\phi,\psi_\parallel$ in poloidal harmonics, we rewrite the gyrokinetic equation for h as

$$\frac{dh}{dt}=-\frac{ie}{T}F_0e^{-i\omega t}\sum_m e^{i(n\zeta-m\theta)}\left\{\omega-\omega_*\left[1+\eta\left(\frac{\epsilon}{T}-\frac{3}{2}\right)\right]\right\}$$
$$\times J_0\left[\phi_m(r)-\left(1-\frac{\omega_d}{\omega}\right)\psi_{\parallel m}(r)\right]. \quad (12)$$

The solution for h is obtained by integrating from $t'=-\infty$ to $t'=t$ along the unperturbed orbit in phase space: $(\mathbf{x}',\mathbf{v}')(t')$ with $(\mathbf{x}',\mathbf{v}')(t'=t)=(\mathbf{x},\mathbf{v})$.

$$h(t)=\tilde{h}e^{i(n\zeta-\omega t)}, \quad (13)$$

$$\tilde{h}=-\frac{ie}{T}F_0\sum_m\int_{-\infty}^{t}dt'e^{i[n(\zeta'-\zeta)-m(\theta'-\theta)-\omega(t'-t)]}$$
$$\times e^{-im\theta}\left\{\omega-\omega_*\left[1+\eta\left(\frac{\epsilon}{T}-\frac{3}{2}\right)\right]\right\}J_0\left[\phi_m(r')-\left(1-\frac{\omega_d(\theta')}{\omega}\right)\psi_{\parallel m}(r')\right]. \quad (14)$$

To be concise, we will not include here the detailed calculation of the orbit integral. The final result is included in Appendix A.

The left hand side of the gyrokinetic moment equation is a complicated function of ϕ_m and $\psi_{\parallel m}$. A newly developed symbolic vector analysis package—General Vector Analysis (GVA)[48]—is used to calculate the analytic expression for it. GVA can perform symbolic vector calculations in any mathematically well-defined coordinate system. In addition, any calculation can be carried out in terms of an asymptotic expansion to any order of a small parameter.

For the tokamak geometry, Eq. (6), and the general 2D expansion, Eq. (8), the left hand side of the gyrokinetic moment equation contains more than 100 terms.

$$-\frac{\partial}{\partial t}\left[\frac{c^2}{4\pi}\nabla\cdot\left(\frac{1}{V_A^2}\nabla_\perp\phi\right)\right]+\frac{c}{4\pi}(\mathbf{B}\cdot\nabla)\frac{(\nabla\times\nabla\times\mathbf{A})\cdot\mathbf{B}}{B^2}$$
$$+(\nabla\times\mathbf{A})_\perp\cdot\nabla\frac{j_{0\parallel}}{B}$$
$$=\frac{c^2}{i\omega 4\pi}\sum_m e^{in\zeta-im\theta-i\omega t}\left(\frac{O_2}{R_0^2}+\frac{O_3}{R_0^3}+\frac{O_4}{R_0^4}\right), \quad (15)$$

where

$$O_3=D_1e^{i\theta}+U_1e^{-i\theta}, \quad (16)$$

$$O_4=D_2e^{2i\theta}+U_2e^{-2i\theta}+SC, \quad (17)$$

where O_2, O_3, O_4, etc. are differential operators acting upon every pair of $\psi_{\parallel m}(r)$ and $\phi_m(r)$. O_2, O_3 and O_4 are $O(\epsilon^0)$, $O(\epsilon^1)$ and $O(\epsilon^2)$, respectively. The O_3 term can be separated into D_1 which couples downward by one poloidal harmonic, and U_1 which couples upward by one poloidal harmonic; the O_4 term can be separated into D_2 which couples downward by two poloidal harmonics, U_2 which couples upward by two poloidal harmonics, and SC which is the self-coupling term. SC can be divided further into the self-coupling term from a straight tokamak SC^s and that from toroidicity SC^t, i.e., $SC=SC^s+SC^t$. Inside every term, there are terms related to $\psi_\parallel$ representing by subscript "ψ" and terms related to ϕ representing by subscript "ϕ." For example, $SC^s=SC^s_\psi+SC^s_\phi$. The detailed expressions for O_2, O_3, O_4, and etc. are listed in Refs. 39, 40, and 48.

Substituting the solution for the distribution function and the result of symbolic vector analysis in the quasineutrality condition and the gyrokinetic moment equation, we obtain the follow ordinary differential equations,

$$\sum_m e^{-im\theta}\begin{pmatrix}A_m^{QN\phi} & A_m^{QN\psi}\\ A_m^{J\phi}+A_m^{F\phi} & A_m^{J\psi}+A_m^{F\psi}\end{pmatrix}\begin{pmatrix}\phi_m''(r)\\ \psi_{\parallel m}''(r)\end{pmatrix}$$
$$+\begin{pmatrix}B_m^{QN\phi} & B_m^{QN\psi}\\ B_m^{J\phi}+B_m^{F\phi} & B_m^{J\psi}+B_m^{F\psi}\end{pmatrix}\begin{pmatrix}\phi_m'(r)\\ \psi_{\parallel m}'(r)\end{pmatrix}$$
$$+\begin{pmatrix}C_m^{QN\phi} & C_m^{QN\psi}\\ C_m^{J\phi}+C_m^{F\phi} & C_m^{J\psi}+C_m^{F\psi}\end{pmatrix}\begin{pmatrix}\phi_m(r)\\ \psi_{\parallel m}(r)\end{pmatrix}=0, \quad (18)$$

where superscripts QN, J, and F refer to the quasineutrality condition, terms on the gyrokinetic moment equation related to the current kink, and terms in the gyrokinetic moment equation involving the distribution function, respectively. A, B, and C are functions of r and θ. Since we have expanded ϕ and $\psi_\parallel$ in poloidal harmonics, it is desirable to have an ordinary differential system in terms of poloidal harmonics. Operating with $1/2\pi\oint d\theta\exp[ip\theta]$ on the above equation, we obtain a coupled ordinary differential equation system of the form

$$\begin{pmatrix}A_{pm}^{QN\phi} & A_{pm}^{QN\psi}\\ A_{pm}^{J\phi}+A_{pm}^{F\phi} & A_{pm}^{J\psi}+A_{pm}^{F\psi}\end{pmatrix}\begin{pmatrix}\phi_m''(r)\\ \psi_{\parallel m}''(r)\end{pmatrix}$$
$$+\begin{pmatrix}B_{pm}^{QN\phi} & B_{pm}^{QN\psi}\\ B_{pm}^{J\phi}+B_{pm}^{F\phi} & B_{pm}^{J\psi}+B_{pm}^{F\psi}\end{pmatrix}\begin{pmatrix}\phi_m'(r)\\ \psi_{\parallel m}'(r)\end{pmatrix}$$
$$+\begin{pmatrix}C_{pm}^{QN\phi} & C_{pm}^{QN\psi}\\ C_{pm}^{J\phi}+C_{pm}^{F\phi} & C_{pm}^{J\psi}+C_{pm}^{F\psi}\end{pmatrix}\begin{pmatrix}\phi_m(r)\\ \psi_{\parallel m}(r)\end{pmatrix}=0. \quad (19)$$

The matrix elements are listed in Appendix B.

The eigenvalue problem for the coupled ODE system is solved using the finite element method. Cubic B-splines are used as the basis functions. After choosing the partition in the radial direction

$$\Delta=\{x_L=x_1<x_2\cdots x_{N-1}<x_N=x_R\}, \quad (20)$$

where x_L and x_R are the left and right boundaries, and N is number of radial knots, we expand the eigenfunctions ϕ_m and $\psi_{\|m}$ in terms of the basis functions $\xi_k(x)$, $(k=1,2,\cdots,N+2)$,

$$\phi_m=\sum_{k=1}^{N+2}\gamma_m^k\xi_k(x),$$
$$\psi_{\|m}=\sum_{k=1}^{N+2}\gamma_{m+M}^k\xi_k(x), \tag{21}$$

where $m=1,2,\ldots,M$; M is the number of poloidal harmonics kept in the system.

The coefficients of the couple ODEs are also expanded in the same manner.[41–43,45,46] The boundary conditions are

$$\phi_m=0 \quad \text{and} \quad \psi_{\|m}=0, \quad \text{for all } m \text{ at } x=x_L,x_R. \tag{22}$$

For the cubic B-splines, there is only one nonzero basis function at either boundary. Therefore, the boundary conditions are

$$\xi_m^1=0 \quad \text{and} \quad \xi_m^{N+2}=0 \quad \text{for all } m. \tag{23}$$

After some algebra, the eigenvalue problem is finally reduced to solving for the eigenfrequencies ω which are roots of

$$f(\omega)=\mathrm{Det}|G_{mm'}^{ij}(\omega)|. \tag{24}$$

We use the Newton method to search for the roots. However, $f(\omega)$ is an extremely complicated function on the complex plane. It is not practical to use the Newton method directly on $f(\omega)$. Tang and Rewoldt[43] used a much more efficient eigenvalue searching method. This method is based on the fact that,

$$f(\omega)=\mathrm{Det}|G_{mm'}^{ij}(\omega)|=\Pi_{i=1}^{2M(N+2)}e_i(\omega), \tag{25}$$

where $e_i(\omega)$ are the ordered eigenvalues of the matrix $G_{mm'}^{ij}(\omega)$,

$$|e_1(\omega)|<|e_2(\omega)|<\cdots<|e_{2M(N+2)}(\omega)|. \tag{26}$$

It is obvious that when $f(\omega)\to 0$, $e_1(\omega)\to 0$. The Newton method is applied to $e_1(\omega)$. Since $e_1(\omega)$ is a much simpler function than $f(\omega)$, we expect much faster convergence. To implement this method, the eigenvalues of the matrix $G_{mm'}^{ij}(\omega)$ have to be solved for, for each guess for ω, and the matching between $e_1(\omega)$ and $e_1(\omega+\delta\omega)$ has to performed interactively.

For a standard setup with 100 radial nodes, and 5 poloidal harmonics for both ϕ and $\psi_\|$, the dimension for the matrix $G_{mm'}^{ij}(\omega)$ is 1020×1020. Running the NAG routine $f02gbf$ on a DEC Personal Workstation 500 a.u. to solve for the eigenvalues and eigenvectors of $G_{mm'}^{ij}(\omega)$ takes about 8 minutes CPU time. Normally, we need less than 10 iterations to get a converged solution. The numerical code is named KIN-2DEM, which can be run either in a global mode or in a radially local mode on a chosen flux surface.

III. KINETIC BALLOONING MODE

To understand the β limit for stability in toroidal systems is an important problem in the area of magnetic confinement. In this respect, high mode number electromagnetic ballooning modes have been an issue for many years, because they are normally unstable for sufficient large β. Theoretical estimates were first obtained for the ideal MHD ballooning mode.[49,50] The kinetic MHD ballooning mode was first introduced by Tang *et al.*[12] to investigate kinetic effects for MHD modes. The kinetic ballooning formalism was shown to be able to recover the MHD ballooning model in certain limits. Moreover, the interaction between kinetic effects and Alfvén waves significantly enriches the physics for the kinetic ballooning mode. Rewoldt *et al.*[4,24] and Tang *et al.*[51] have numerically implemented the kinetic MHD ballooning theory and carried out extensive numerical studies. The implemented one-dimensional numerical code using the high- n ballooning representation is called the FULL code.

To leading order, the ballooning mode is a local mode on a chosen flux surface, with short perpendicular and long parallel wavelength. Usually, the ballooning mode is studied by using the WKB type of ballooning representation,

$$\begin{pmatrix} f \\ \phi \\ \psi_\| \end{pmatrix}=\begin{pmatrix} \tilde{f} \\ \tilde{\phi} \\ \widetilde{\psi_\|} \end{pmatrix}e^{i\chi}, \tag{27}$$

where χ carries the short wavelength structure in the perpendicular direction, and $\mathbf{b}\cdot\nabla\chi=0$. $\tilde{f}$, $\tilde{\phi}$, and $\widetilde{\psi_\|}$, on the other hand, contain only slow variation structure. In toroidal geometry, f, ϕ, and $\psi_\|$ actually represent a ''quasimode,''[52] whose domain in the extended poloidal angle is $(-\infty, +\infty)$.

In our two-dimensional calculation, we do not use the ballooning representation. But the ballooning mode can be represented by radially local modes in the two-dimensional analysis. By keeping a wide enough poloidal spectrum centered at $m=nq(r)$, we are able to describe the basic features of ballooning modes. First, the kinetic ballooning mode is indeed a localized mode around some flux surface; second, $\mathbf{b}\cdot\nabla\chi=0$, the basic feature of the kinetic ballooning mode, is equivalent to the condition $m\approx nq(r)$; and the slow variation along the field line is included by the poloidal spectrum.

We have calculated the local eigenmode using the KIN-2DEM code for Tokamak Fusion Test Reactor (TFTR) shot No. 49982S05 at $t=4.00$ seconds, and benchmarked the result against the high-n ballooning results from the FULL code. It is found from the FULL code calculation that the maximum growth rate is located at $r/a=0.54$. We therefore have performed the radially local calculations at the same flux surface using the KIN-2DEM code. The equilibrium profiles for density, q, and temperature are plotted in Fig. 2. In order to obtain a substantial growth rate, the plasma density has been scaled up by a factor of 13.75 such that $\beta=2.44\%$ at $r/a=0.54$.

In Fig. 3, we plot the real parts of the eigenfrequencies ω_r and the growth rates γ against the toroidal mode number n. It can be seen from the figures that the KIN-2DEM code

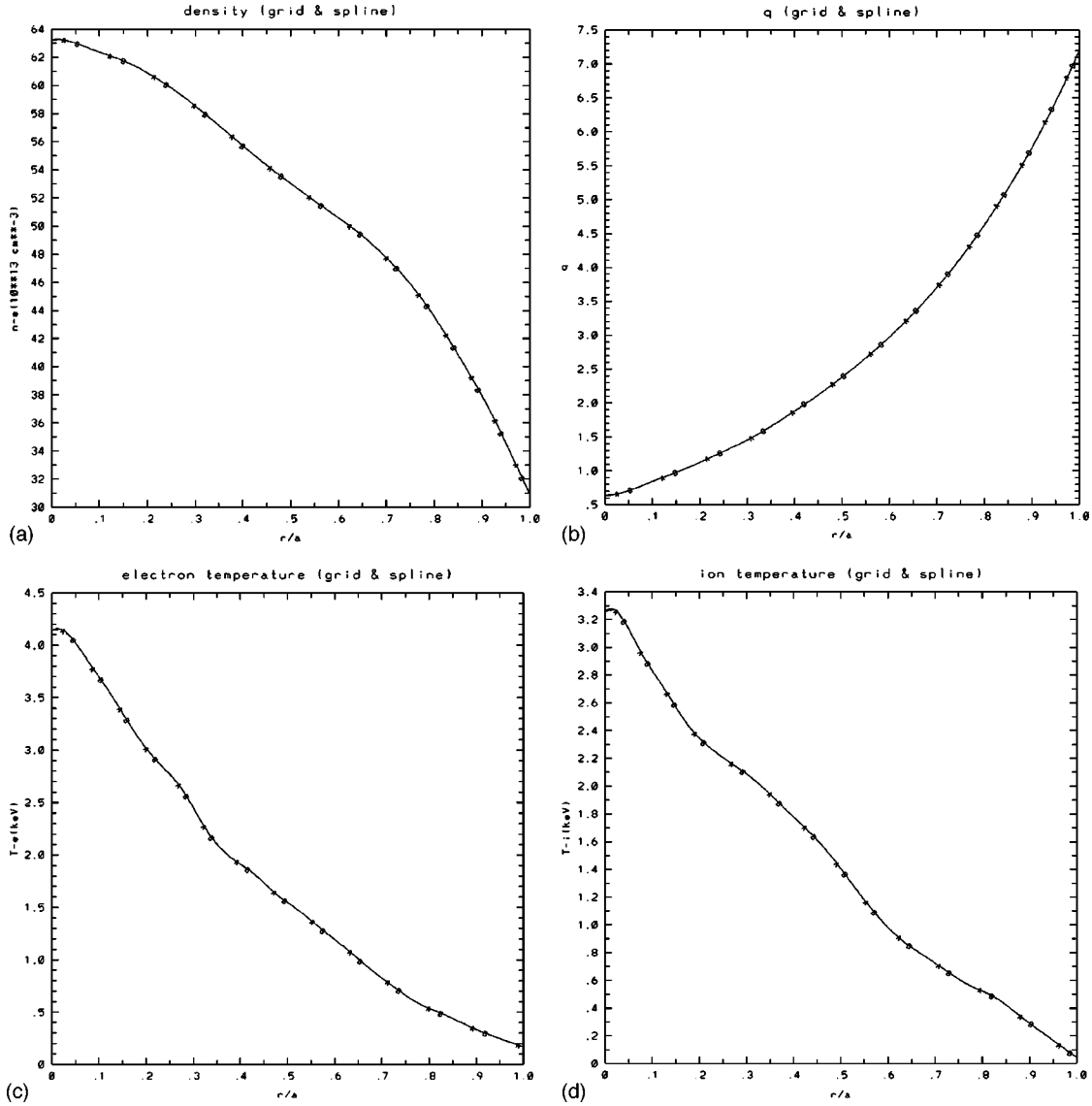

FIG. 2. Equilibrium profiles for TFTR Shot No. 49982S05 at $t=4.00$.

results agree with the FULL code results reasonably well. The best agreement is for medium n, i.e., $n=15\sim45$. This is the consistent with the fact that for low n the KIN-2DEM code is more accurate, while for high-n the FULL code is more accurate. However, for this case it appears that there is no region of overlap in n where both codes are at their most accurate.

Plotted in Fig. 4 is the mode structure in the poloidal

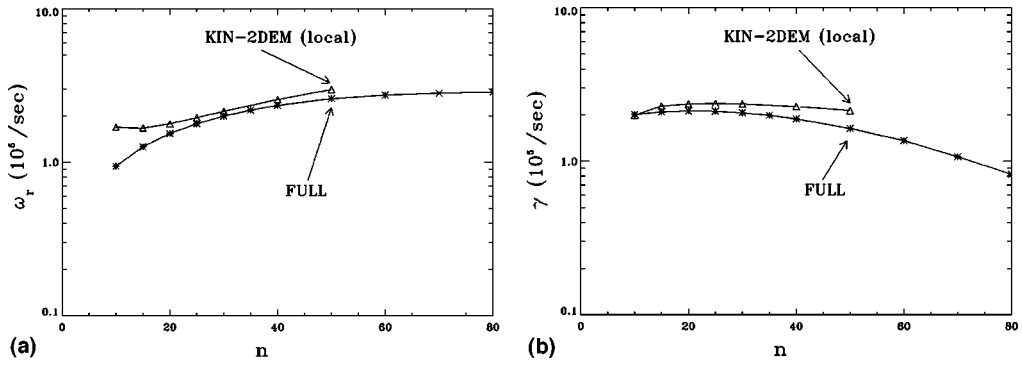

FIG. 3. Kinetic ballooning mode. Real frequency and growth rate are plotted against n for TFTR shot No. 49982S05 at $t=4.00$, $r/a=0.54$, and $\beta=2.44\%$. Results from the KIN-2DEM code and the FULL code are compared. (a) Real Part. (b) Growth Rate.

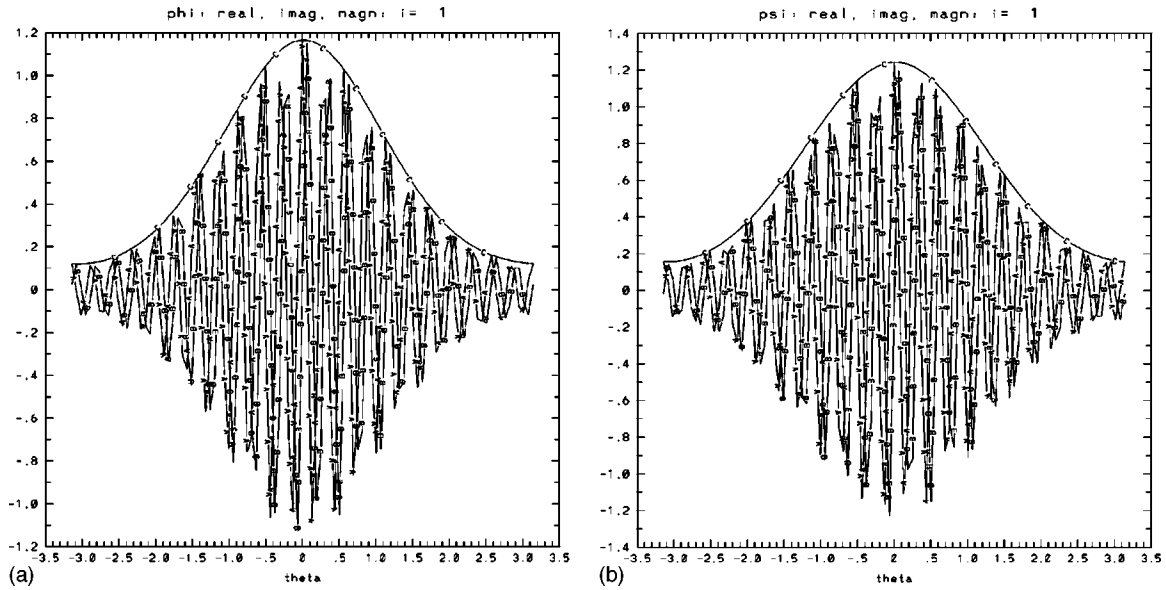

FIG. 4. Kinetic ballooning mode structure in θ. The ballooning structure is evident from the plots of ϕ and $\psi_{\|}$ calculated by the KIN-2DEM for $n=30$. The equilibrium is for TFTR shot No. 49982S05 at $t=4.00$, $r/a=0.54$, and $\beta=2.44\%$. (a) ϕ. (b) $\psi_{\|}$.

direction calculated by the KIN-2DEM code. The toroidal mode number n is 30. The ballooning structure is evident from the plot: the mode is strong around $\theta=0$ and weak around $\theta=\pi$.

IV. INTERNAL KINK MODE

The internal kink mode in tokamaks is driven by the equilibrium inhomogeneities, particularly the current density gradient. It has been studied extensively for many years. While the ideal MHD internal kink mode in a straight tokamak (screw pinch) is well-known,[36,37,53] the internal kink mode in toroidal geometry is a quite subtle problem. In 1975, Bussac *et al.*[38] concluded that toroidicity is a stabilizing factor and that the internal kink mode is stable when β is sufficiently low. One year latter, Pao[54] obtained the opposite conclusion that unstable $(m=1,\ n=1)$ internal kink modes in a screw pinch are also unstable in toroidal geometry with even greater growth rates. Galvao *et al.*[55] in 1978 showed that toroidicity can be either stabilizing or destabilizing in different parameter regions. Numerical results by Kerner *et al.*,[56] using circular flux surfaces and parabolic pressure profiles, agreed with Bussac *et al.*'s conclusion. Extensive numerical studies, including all the important geometrical effects, were conducted by Manickam.[44]

Moreover, Pao pointed out that the linear growth rate from the classical MHD model for the internal kink mode in a screw pinch is 4–7 times greater than the experimental observation.[54] Investigation of the internal kink mode using other models than MHD provoked more interests. Strauss concluded that, in circular tokamaks, the internal kink modes are stable or marginally stable in his reduced MHD model, and these modes are favorable for confinement.[57,58] Only in a straight tokamak with a rectangle wall did Strauss find the internal kink mode to be unstable. Naitou *et al.*[59] reached the same conclusion from a gyrokinetic particle simulation. Using their reduced model, Hazeltine and Meiss[60] found that there are no unstable kink modes for a cylindrical model with a conducting wall.

Such subtleties arise from the fact that the growth rate for the internal kink mode is $O(\epsilon^2)$ smaller than that for the external kink mode. For the same reason, the pure MHD internal kink mode may not be important after all. The internal kink mode is interesting only because of its potential to interact with other kinetic components existing in the tokamak plasma. The kinetic components in a modern tokamak include both the energetic particles and the kinetic effects of the background plasma. The fishbone mode, strongly correlated with losses of injected energetic beam ions, is dominantly an $(m,n)=(1,1)$ mode destabilized by the trapped energetic ions.[7]

An analytical study of internal kink modes using the gyrokinetic model developed here has been carried out in Refs. 39 and 40. Even though analytic calculations can bring us some physical insight, numerical analysis is indispensable for the internal kink mode in toroidal geometry. In this paper, we focus on numerical results from the KIN-2DEM code, and especially investigate the kinetic effects due to the background plasma on the internal kink modes. We have compared numerical results from the KIN-2DEM code and the PEST code for a test case. Growth rates are calculated for a family of equilibria generated by the PEST code. Different equilibrium profiles are characterized by different $q_0 \equiv q(r=0)$. The plasma density, pressure, and q profiles for the equilibrium with $q_0=0.90$ are plotted in Fig. 5. Other plasma parameters are $B_0=4.605$ T, $R_0=245$ cm, and $a=24.5$ cm. Also plotted in Fig. 5 is the mode structure for the internal kink mode calculated by the KIN-2DEM code.

In Fig. 6, the growth rates calculated by the PEST code and the KIN-2DEM code are plotted against q_0. In this calculation, all the kinetic effects inside the KIN-2DEM code are turned off. From Fig. 6, the KIN-2DEM code results

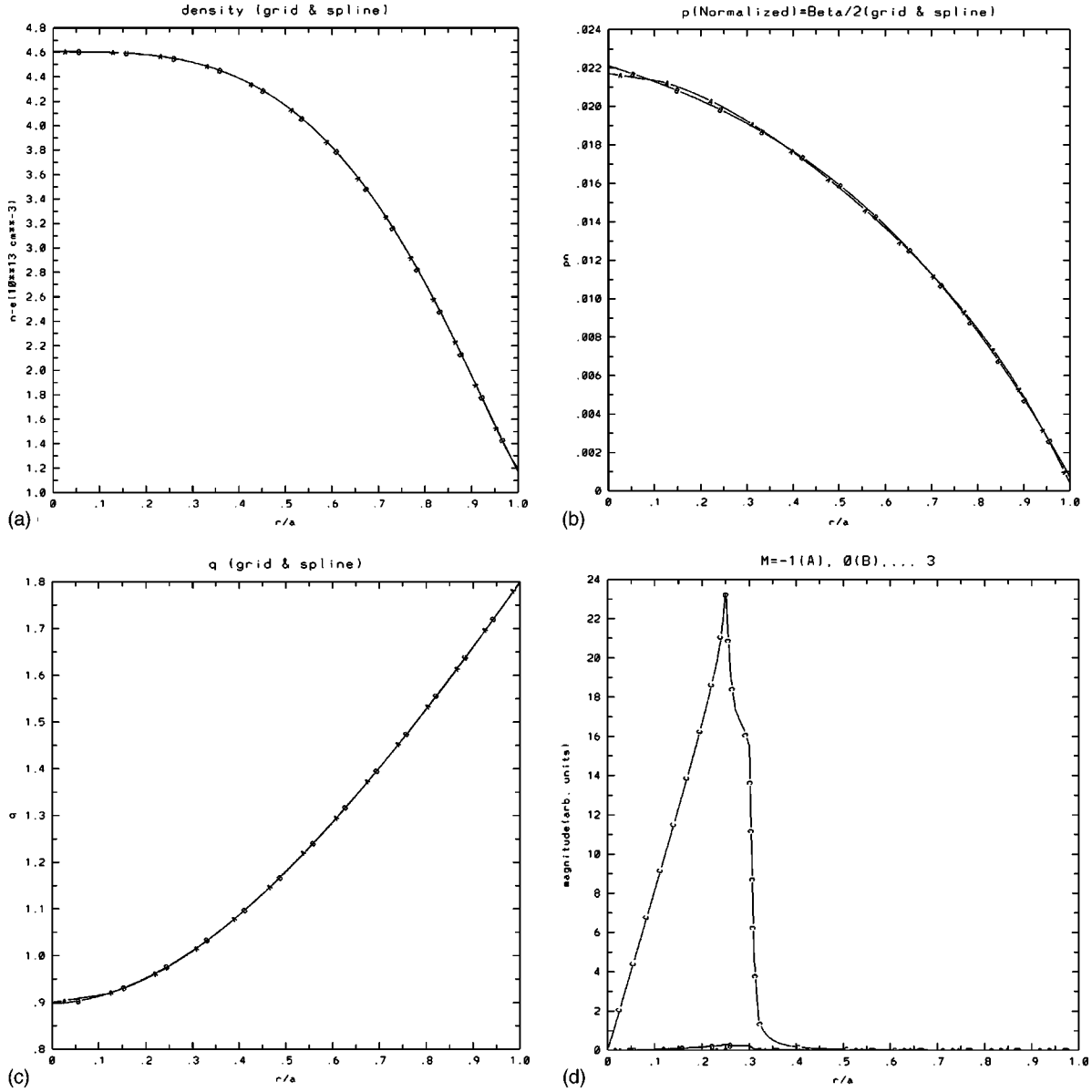

FIG. 5. Equilibrium profiles and mode structure for the case $q_0=0.9$. (a) Density. (b) Pressure. (c) $q(r)$. (d) Mode structure, $\phi(r)=\psi_{\|}(r)$.

agree with the PEST code results. The small discrepancy can be mainly attributed to the Shafranov shift neglected in the model equilibrium assumed by the KIN-2DEM code. In this case, the relative Shafranov shift calculated by the PEST code is about 20%.

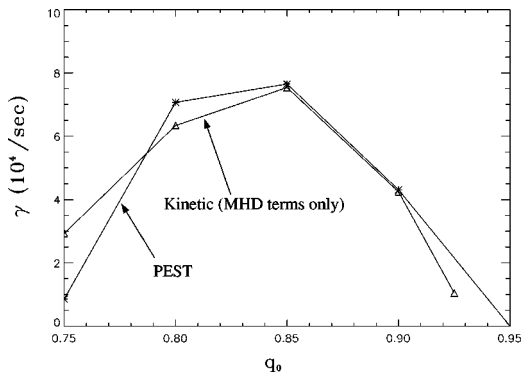

FIG. 6. Growth rates vs q_0. KIN-2DEM code agrees with the PEST code.

The q_0 dependence of the growth rate γ can be explained by the basic features of the internal kink mode.[61] γ peaks around $q_0=0.85$, and γ increases as q_0 increases when $q_0<0.85$. This is because, when q_0 increases, r_s decreases, and the effective toroidicity r_s/R_0 decreases. Since toroidicity is generally stabilizing, the growth rate increases. However, this trend has to be reversed somewhere because, if $q_0>1$, the mode is stable to leading order. Thus, after some critical value, when q_0 approaches 1, the growth rate decreases. This critical value for q_0 is where the growth rate reaches its maximum. In the current case, the critical point is $q_0=0.85$. From another point of view, this descending feature of the γ versus q_0 curve when $q_0>0.85$ is also related to the r_s variation. When $q\to 1$, $r_s\to 0$, then $\omega^2\sim\delta W\to 0$, because the trial function vanishes when $r>r_s$.

As discussed before, the internal kink mode is interest-

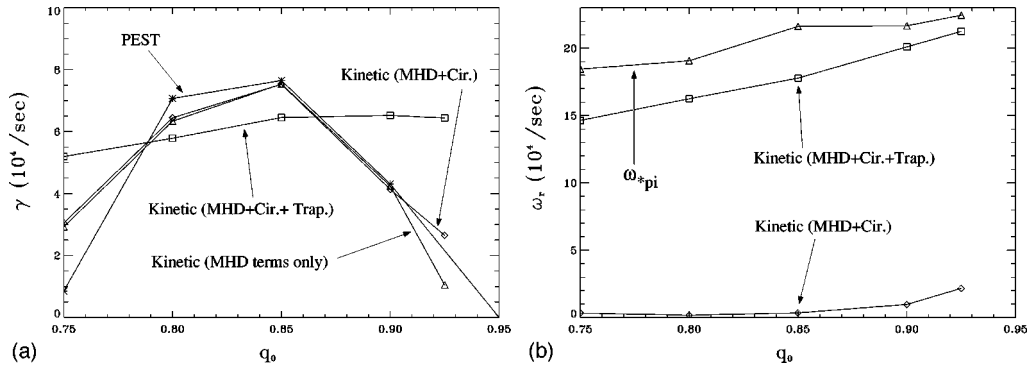

FIG. 7. Kinetic effects on internal kink mode. Trapped ions flatten the γ vs q_0 curve, and bring significant real parts into the eigenfrequencies. (a) Growth rates. (b) Real frequencies.

ing only because of its potential to interact with the kinetic components existing in the tokamak plasma. In this section, we present our numerical results on the kinetic effects due to the background plasma.

In Fig. 7, the growth rates and the real parts of the eigenfrequencies are plotted for cases with no kinetic effects, with only kinetic effects due to circulating particles, and with kinetic effects due to both circulating and trapped particles.

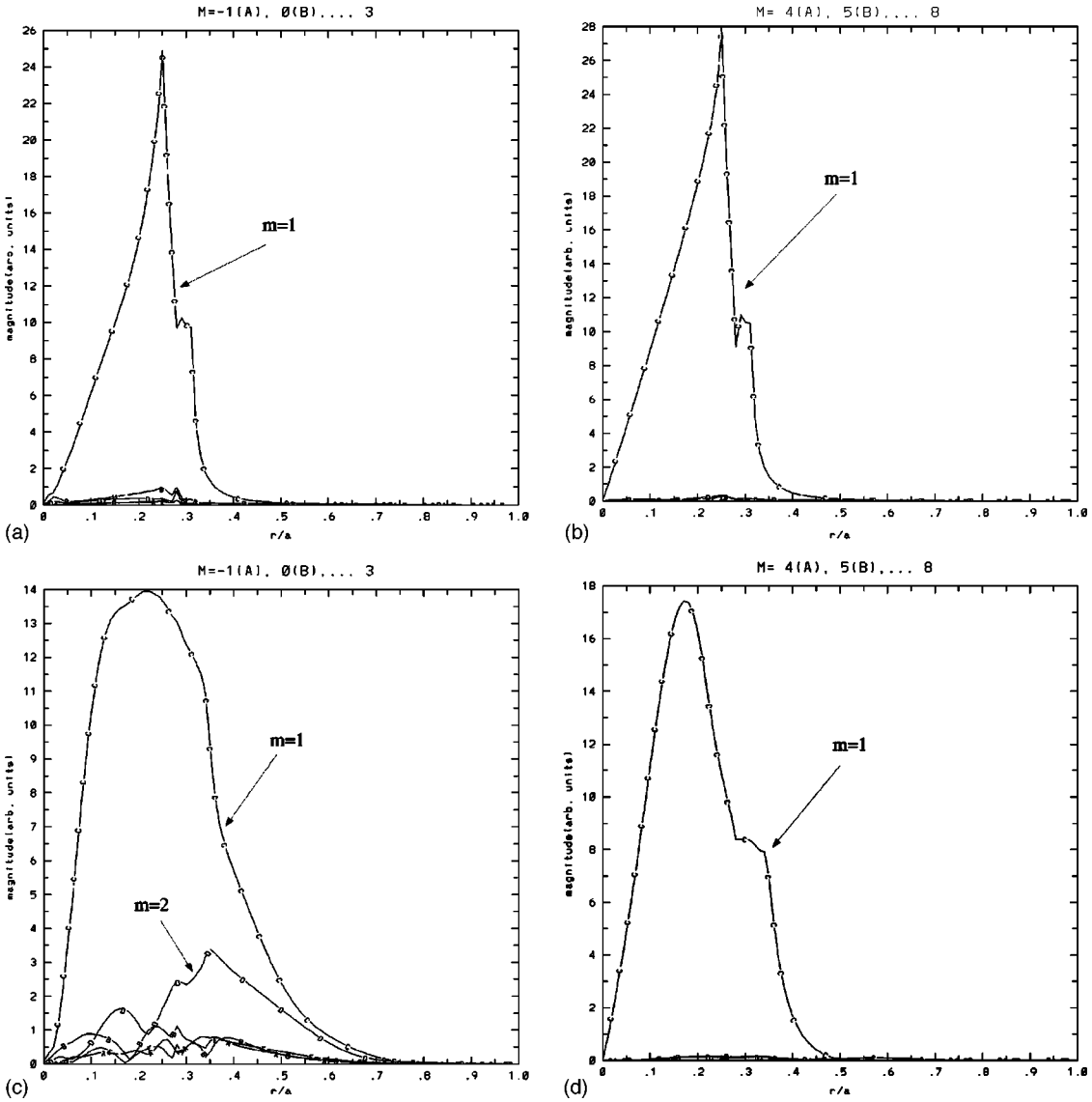

FIG. 8. Kinetic effects on internal kink mode. The mode structure is not significantly affected by the circulating particles, but is modified by the kinetic effects due to trapped ions. (a) $\phi(r)$ with circulating particles only. (b) $\psi_{\parallel}(r)$ with circulating particles only. (c) $\phi(r)$ with circulating and trapped particles. (d) $\psi_{\parallel}(r)$ with circulating and trapped particles.

The equilibria are the same as in the previous section. The mode structures under the influence of the kinetic effects for the case $q_0=0.9$ are illustrated in Fig. 8.

For the case we are studying, the kinetic effects due to circulating particles are small. The dominant kinetic effects are from the trapped ions. This observation accords with the following estimates for the kinetic resonances. The ion temperature for the equilibrium with $q_0=0.9$ is $T_i\sim 25$ keV. Thus,

$$\omega_{ti}\sim \frac{v_i}{R_0 q}\sim 6\times 10^5/\mathrm{s}\gg \omega\sim 1\times 10^5/\mathrm{s}. \tag{28}$$

From Eq. (B3) the kinetic resonances between waves and the circulating particles are controlled by the factor

$$\frac{(\omega-\omega_{*i}^T)\omega}{\omega^2-(n+S)^2\omega_{ti}^2}.$$

$(n+S)^2$ is normally nonzero for any n at most radial locations. Consequently, there are no effective kinetic resonances for the circulating ions. However, for the trapped ions, the physical picture is different. From Eqs. (B1), (B2), and (B3), the trapped particle resonance is controlled by the factor

$$\frac{\omega-\omega_{*i}^T}{\omega-\omega_D^{(0)}-n\omega_{bi}}.$$

The trapped ion resonances are much stronger by two reasons. First,

$$\omega_{bi}\sim \sqrt{\epsilon}\omega_{ti}\sim 2\times 10^5/\mathrm{s}\gtrsim \omega. \tag{29}$$

When $\omega_D^{(0)}$ is small, we expect strong kinetic resonances between the wave and the trapped ions. Second,

$$v_{di}\sim \frac{\rho_i}{R_0}v_{thi}\sim 3\times 10^5\ \mathrm{cm/s}, \tag{30}$$

$$\omega_D^{(0)}\sim \frac{v_{di}}{r}\sim 1\times 10^5/\mathrm{s}. \tag{30}$$

When $n=0$, ω_{bi} does not enter, and the resonance factor is $(\omega-\omega_*^T)/(\omega-\omega_D^{(0)})$. There is strong resonance between the wave and the time-averaged drift motion of the trapped ions. This $n=0$ resonance exists even when $\omega_{bi}\gg\omega$. In the current case, ω_{bi}, $\omega_D^{(0)}$, and ω are comparable, and the trapped ions' drift motions resonate with the internal kink mode and significantly modify the eigenfrequency and the mode structure. For electrons, the kinetic effects are not important because $\omega_{be}\gg\omega$ and $\omega_{te}\gg\omega$. The trapped electrons can contribute to the kinetic resonances only when $n=0$, considering the fact that $\omega_{De}^{(0)}\sim\omega_{Di}^{(0)}\sim\omega$. But for the A and B matrices, the contribution from trapped electrons is much smaller than that from trapped ions, because the A and B matrices are proportional to $\rho_{\theta j}^2$ and $\rho_{\theta j}$, respectively.

The kinetic resonances due to the trapped ions also change the q_0 dependence of the growth rate. From Fig. 7, the peaked γ versus q_0 curve is flattened by the trapped ion resonances. In the previous section, we explained that the peaked γ versus q_0 curve is the result of r_s variation. When the trapped ions are present in the system, the radial variation is averaged out by the trapped ions because of their finite banana width in the radial direction. Since the banana width for ions is much bigger than that for electrons, this averaging effect is only prominent for trapped ions. This trapped ion effect is evident from the real parts of the eigenfrequencies as well. It is well-known that ideal MHD unstable modes do not have real parts in their eigenfrequencies. We see that circulating particles do not change this characteristic very much, whereas the trapped ions bring significant real parts into the eigenfrequencies.

From Fig. 8, it is clear that the mode structure is not significantly affected by the circulating particles, but is modified by the kinetic effects due to the trapped ions. This is consistent with the conclusion we draw from the γ versus q_0 curve and the ω_r versus q_0 curve. In addition, when only the circulating particles are included, $\phi(r)\approx\psi_\parallel(r)$, that is $E_\parallel\approx 0$. This is one of the basic features of ideal MHD. We see that trapped ions change this feature and bring in $E_\parallel$.

V. TAE

It is found that TAEs can be destabilized by alpha particles and other hot particles when their pressure is high enough.[9,10,62,63] Experimental and theoretical studies shown that unstable TAEs, driven by energetic particles, can lead to 80% of the energetic particle transport in some present tokamaks.[11] Besides reducing the plasma β, loss of energetic particle power through TAEs could result in serious wall damage, impurity flux, major operational control problems, and even a failure to sustain ignition. In this section, the new gyrokinetic system developed will be used to study the TAEs. This represents the first fully kinetic model for the TAEs. More importantly, the destabilization of the TAE by energetic particles and the background damping will be investigated nonperturbatively. Compared with previous hybrid models and δW estimates for the growth rate and damping mechanism,[10,18–20] the fully kinetic model is more comprehensive and self-consistent. In this section, the numerical results from the KIN-2DEM code and the NOVA-K code[10,18–20] will be compared.

First, we give a numerical example of the TAE calculated by the KIN-2DEM code, and compare the results with the those of the NOVA-K code. We choose the following model equilibria:

$$\begin{aligned} &R_0=300\sim 500\ \mathrm{cm},\quad a=90\ \mathrm{cm},\quad B_0=5\ \mathrm{T},\\ &n(\psi)=n_0=5\times 10^{13}/\mathrm{cm}^3,\quad q(\psi)=1.05+0.6\psi, \end{aligned} \tag{31}$$

where ψ is the normalized poloidal flux, with $\psi=0$ at the magnetic axis and $\psi=1$ at the plasma boundary. For the equilibrium model with circular concentric flux surfaces, there is an one–one relationship between ψ and minor radius r, which is the radial coordinate used in the KIN-2DEM code. In particular, for the family of q profiles $q(\psi)=q^{(0)}+q^{(1)}\psi$, the relation between the normalized minor radius r and ψ is

$$r^2\left(1+\frac{q^{(1)}}{3q^{(0)}}\right)=\psi+\frac{q^{(1)}}{3q^{(0)}}\psi^3. \tag{32}$$

The solution for ψ in terms of r is

$$\psi(r)=-\left(\frac{2}{b+c}\right)^{1/3}+\frac{1}{3a}\left(\frac{b+c}{2}\right)^{1/3},$$

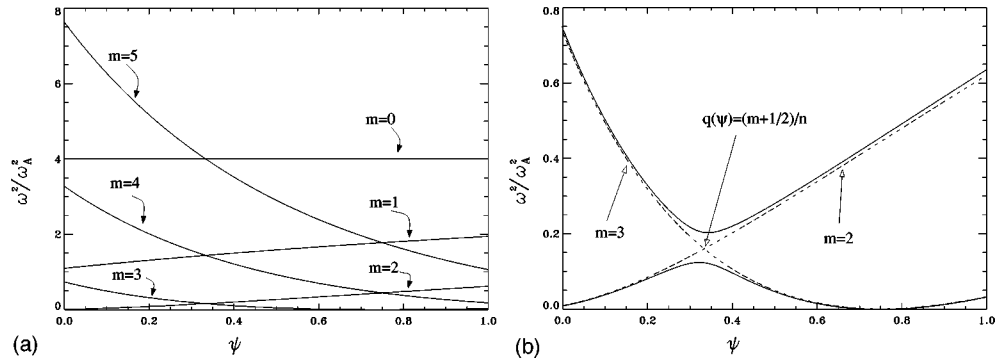

FIG. 9. Shear Alfvén continuum. (a) Continuum without coupling. (b) Continuum gap for $m=2$ and $m=3$ harmonics.

$$b=27a^2(1+a)r^2,$$
$$c=\sqrt{108a^3+729a^4(1+a)^2r^4}, \tag{33}$$
$$a=\frac{q^{(1)}}{3q^{(0)}}.$$

Background pressure is neglected, to be consistent with the circular concentric flux surfaces assumed by the KIN-2DEM code. We look at $n=2$ modes. Shown in Fig. 9(a) is the continuous spectrum given by $\omega^2=\omega_A^2k_\parallel^2$ without toroidicity-induced coupling for the case of $R_0=400$ cm. The strongest

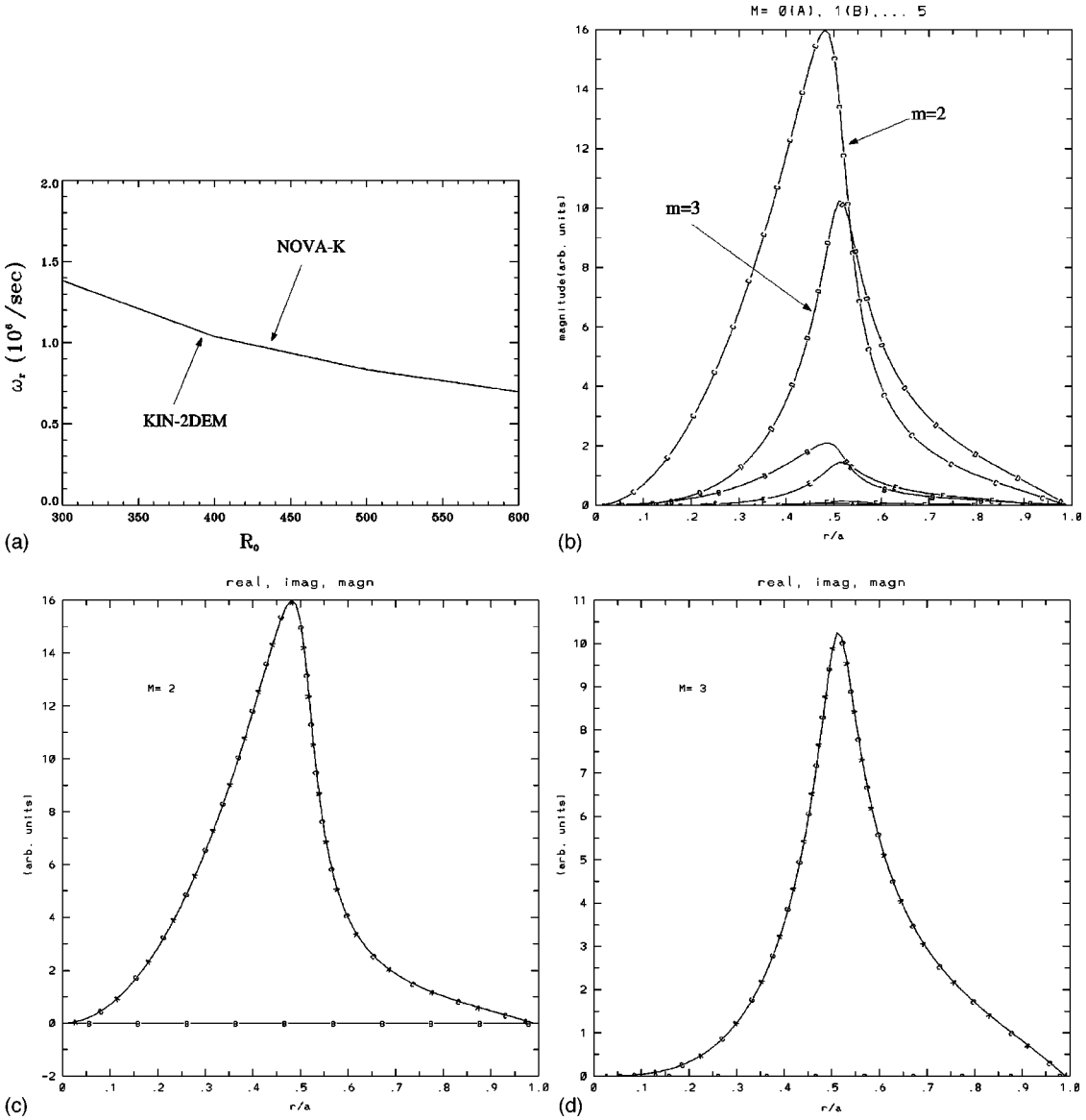

FIG. 10. Even TAE. (a) Eigenfrequency. (b) Mode structure, all harmonics. (c) Mode structure, $m=2$. (d) Mode structure, $m=3$.

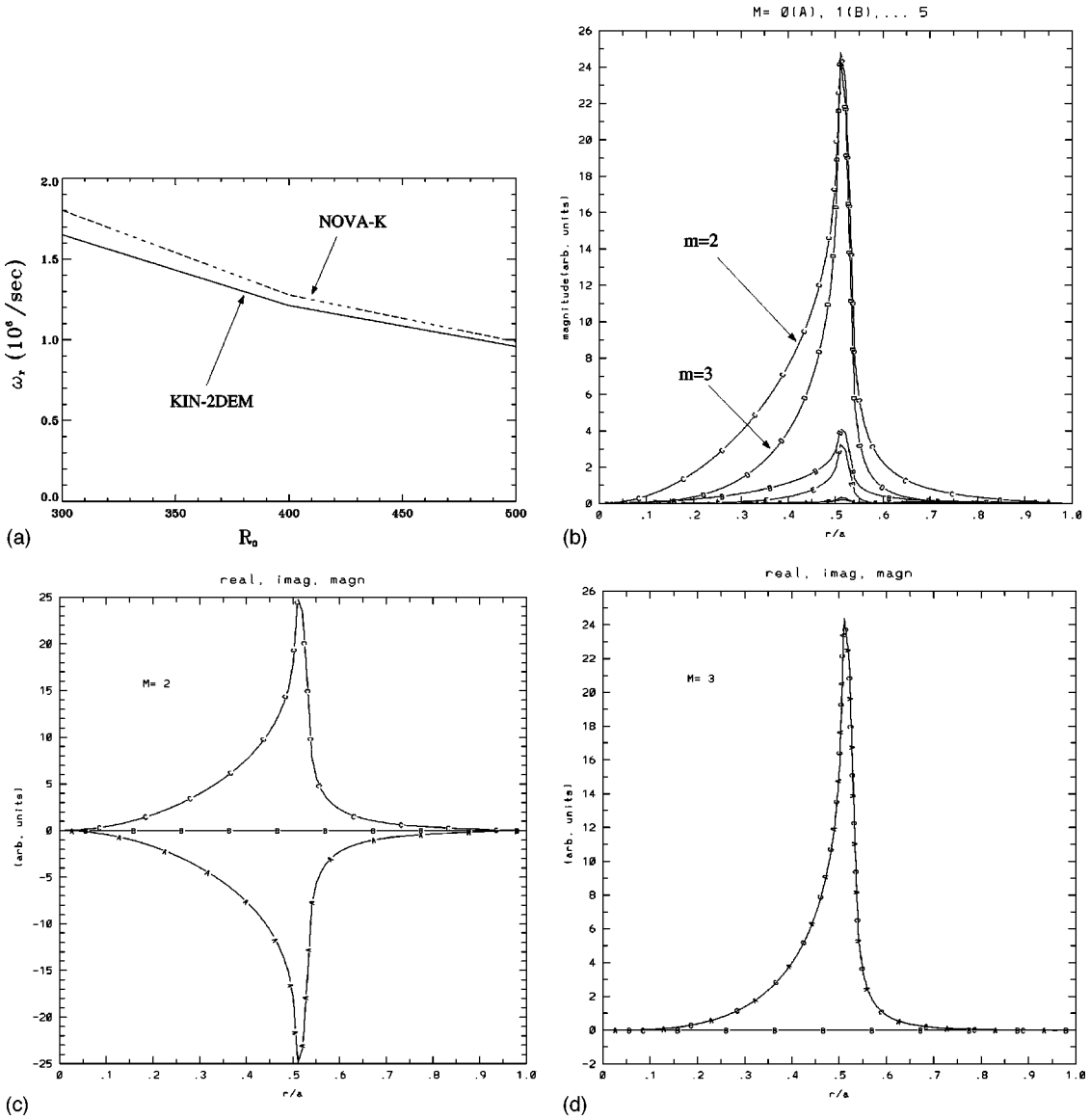

FIG. 11. Odd TAE. (a) Eigenfrequency. (b) Mode structure, all harmonics. (c) Mode structure, $m=2$. (d) Mode structure, $m=3$.

toroidicity-induced coupling occurs at the flux surface where $q(\psi)=5/4$ between the $m=2$ and $m=3$ harmonics. Plotted in Fig. 9(b) are the continua for the $m=2$ and $m=3$ harmonics without and with coupling.

Numerically, two TAEs are found in the gap. The one with lower frequency has the same phase for the dominant $m=2$ and $m=3$ harmonics, and is called the even mode. The other one with higher frequency has opposite phases for the dominant $m=2$ and $m=3$ harmonics, and is called the odd mode. In Figs. 10(a) and 11(a), the eigenfrequencies from the KIN-2DEM code and the NOVA-K code are plotted against R_0 for both the even and the odd mode. The results from the KIN-2DEM and the NOVA-K codes agree with each other very well. Drawn in Figs. 10(b), 10(c), and 10(d) are the mode structures of the even mode for the case of $R_0=400$ cm. The counterparts for the odd mode are drawn in Figs. 11(b), 11(c), and 11(d). The characteristics of the even and odd modes are clear from the plots. The dominant harmonics are $m=2$ and $m=3$, and the harmonics peak at the radial location where $q=(1/n)(m+\frac{1}{2})$, as predicted in the analytic model.

In the rest of this section, we study numerically the kinetic destabilization of the TAEs by energetic particles, as well as the damping due to the background plasma. Compared with the existing hybrid models,[10,18–20] the fully kinetic approach developed here is more self-consistent and comprehensive. Compared with the δW calculation for the growth rate and background damping widely used in the hybrid models, the eigenvalue calculation is nonperturbative and more accurate. To investigate the destabilization of the TAEs, we introduce a third species, of energetic hydrogen ions, into the system. The fast ions are assumed to be Maxwellian with a constant temperature profile. The pressure profile for the hot particles is

$$p_h=p(0)e^{-\psi/0.09}. \tag{34}$$

The domains of variation for the hot particle thermal velocity v_h and β_h at the magnetic axis are

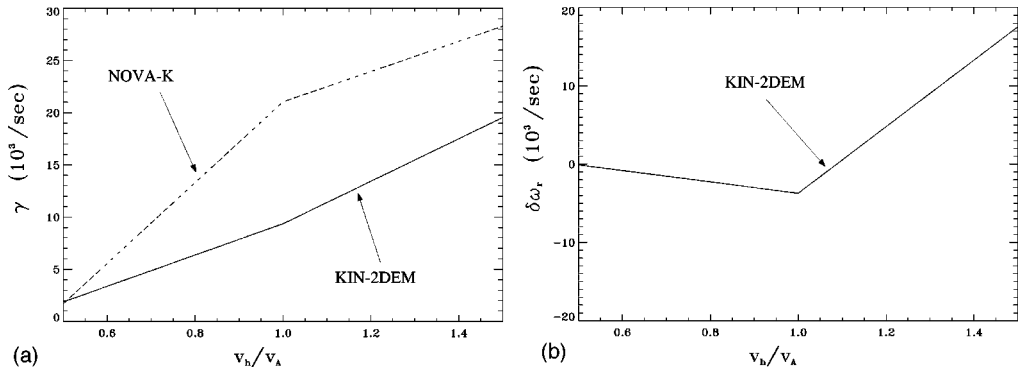

FIG. 12. Destabilization of TAE by hot particles. The even mode for the case $R_0=400$ cm is destabilized by energetic particles with different v_h. (a) Growth rate. (b) Real frequency.

$$0.5 \leqslant \frac{v_h}{v_A} \leqslant 1.5, \quad 0 \leqslant \beta_h \leqslant 1.0. \tag{35}$$

To include the background damping, the background temperature profile is assumed to be

$$T_e = T_i = 0.5(1-\psi)^2 \ \text{keV}. \tag{36}$$

We will look at the destabilization of the even mode for the case $R_0=400$ cm. Shown in Fig. 12(a) is the growth rate versus v_h calculated by the KIN-2DEM code and the NOVA-K code; in Fig. 12(b) is the change in the real frequency calculated by the KIN-2DEM code. Since the NOVA-K code use a perturbative δW calculation, the perturbation in the eigenfrequency can only be pure imaginary or pure real. In the current case, only the growth rate is perturbed. The agreement between the KIN-2DEM code and the NOVA-K code varies with v_h/v_A. The best agreement is at $v_h/v_A=0.5$, while the difference reaches its maximum at $v_h/v_A=1.0$. This discrepancy is mainly due to the difference in the basic models. The NOVA-K code is based on a hybrid model, and assumes that the perturbation due to hot particles is small. The perturbation in eigenfrequency is obtained from δW using the unperturbed ideal MHD mode structure. The KIN-2DEM code, on the other hand, is a fully kinetic, nonperturbative code. All plasma species are treated equally, and the eigenfrequency, containing both real and imaginary parts, is calculated by solving the eigenvalue problem. The eigenfunction is obtained self-consistently as well.

In Fig. 13(a), the growth rate is plotted against β_h for the case of $v_h/v_A=1.5$. For the NOVA-K code, δW_h is proportional to the density of hot particles. When β_h is increased by increasing the hot particle density, the growth rate increases linearly. Moreover, in the NOVA-K code, the background damping is fixed, and is represented by a negative offset when $\beta_h=0$. In the KIN-2DEM code, the eigenvalue is calculated separately for each β_h value. Therefore it can used to test the linear scaling of γ with respect to β_h. From Fig. 13(a), we see that the linear scaling is approximately valid. An interesting observation is that the linear scaling is less accurate for smaller β_h where the background stabilization is comparable to the hot particle destabilization. This indicates that background damping is not just a simple offset of the growth rate, and the background stabilization and hot particle destabilization are indeed coupled together. It also reflects the fact that the underlying theory for the δW estimate—the energy principal and the variational principle are not accurate for modes with relatively strong kinetic resonances.

VI. CONCLUSIONS AND FUTURE WORK

In 2D tokamak geometry, we have developed a numerical solution method for the electro-magnetic gyrokinetic system. The gyrokinetic equation is solved for the distribution function in terms of the perturbed field by integrating along

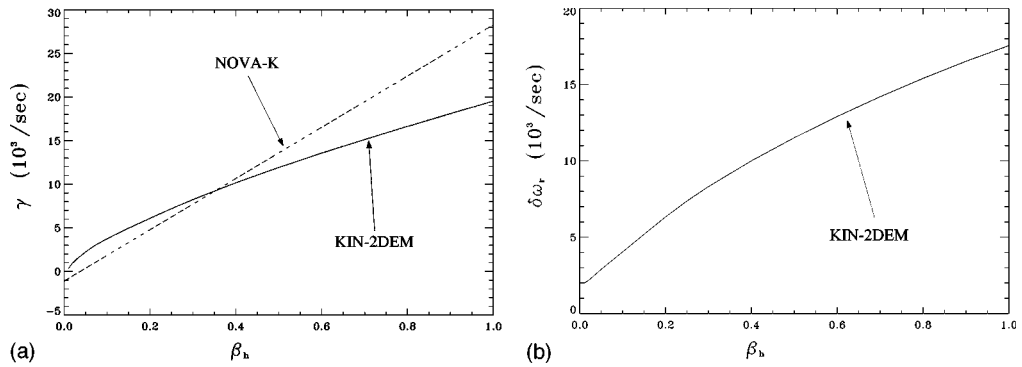

FIG. 13. Destabilization of TAE by hot particles. The even mode for the case $R_0=400$ cm is destabilized by energetic particles with $v_h/v_A=1.5$. The linear scaling of γ with respect to β_h is approximately valid. (a) Growth rate. (b) real frequency.

unperturbed orbits. The solution is substituted back into the gyrokinetic moment equation and the gyrokinetic Poisson equation. When the boundary conditions are incorporated, an eigenvalue problem is formed. A newly developed computer algebra package, General Vector Analysis, is used to efficiently carry out the complicated vector calculus. The eigenmode is Fourier decomposed in the poloidal direction, and the coupled second order ODE system in the radial direction is solved by a finite element method. The resulting numerical code, KIN-2DEM, can operate in a radially global mode as well as in a radially local modes on a chosen flux surface. As an example of such a local calculation, KIN-2DEM has recovered the kinetic ballooning mode, and the numerical results agree with those calculated by the high-*n* FULL code. The KIN-2DEM code has also been applied to the internal kink mode. This represents the first fully kinetic model for the internal kink mode. Ideal MHD results for both a straight tokamak and in toroidal geometry are recovered in validation tests. The numerical results from the KIN-2DEM code agree well with those from the well-established PEST code. It is also discovered that trapped ions can change the characteristics of the growth rate γ versus central safety factor q_0 curve, and introduce significant real parts into the eigenfrequencies. In addition, the TAE mode has been recovered from the new gyrokinetic system of equations. As in the case for the internal kink mode, this represents the first fully kinetic model for the TAE modes. The numerical results from the KIN-2DEM code and the NOVA-K code agree very well. It is found that energetic (beam) hydrogen ions can destabilize the TAE modes. On this problem, the agreement between the KIN-2DEM code and the NOVA-K code varies with v_h/v_A. The best agreement is at $v_h/v_A=0.5$, while the difference reaches its maximum at $v_h/v_A=1.0$. This discrepancy is mainly attributed to the differences in the basic models. The linear scaling of the growth rate γ with respect to the hot particle β_h assumed by the hybrid models is tested by the KIN-2DEM code. It is found that the linear scaling is approximately valid. However, it is less accurate when the background damping is comparable to the hot particle destabilization.

The current version of the KIN-2DEM code is an eigenvalue code for shear Alfvén waves in a circular concentric model equilibrium. It is of practical interest to extend the code to general numerically calculated equilibria so that extra geometric effects, such as the Shafranov shift, can be included in the analysis. Again, the computer algebra package for vector analysis is expected to be a powerful tool in the process of the extension. Adopting realistic equilibria will help the KIN-2DEM code to improve its accuracy in addressing the kinetic MHD problems for real experimental cases. Moreover, adding the compressional component of the magnetic perturbation and the perpendicular dynamics will extend the code to a wider range of modes, including compressional Alfvén waves and cyclotron waves.[23]

A gyrokinetic model for an equilibrium with shear flow has been an active research topic in tokamak physics recently. Nonlinear gyrokinetic systems have been derived by Artun *et al.*,[45,46] Brizard,[64] and Hahm.[65] Normally, the gyrokinetic equation is derived in the shear flow frame, where extra inertial forces appear. An alternative approach is to represent the shear flow by a shifted equilibrium Maxwellian distribution in the lab frame, where the functional form of the gyrokinetic equation is not affected by the shear flow. The latter point of view probably is more general, because, besides the shear flow, we can put more equilibrium properties into the equilibrium distribution function. This method is a special case of the Chapman–Enskog-like approach proposed by Callen,[66–68] which separates the distribution function into the dynamic Maxwellian f_d and the kinetic distortion F.

$$f(\mathbf{x},\mathbf{v},t)=f_d+F, \tag{37}$$

where

$$f_d=n\left(\frac{m}{2\pi T}\right)^{3/2}e^{-\frac{mu^2}{2T}}\left[1+\frac{2}{v_t^2}\mathbf{u}\cdot\left(-\frac{2}{5nT}\mathbf{q}\right)L\right],$$
$$L=\frac{5}{2}-\frac{mu^2}{2T},\quad \mathbf{u}=\mathbf{v}-\mathbf{V}, \tag{38}$$

and n, T, $\mathbf{V}$, and $\mathbf{q}$ are functions of $\mathbf{x}$ and t. F represents the kinetic part of f beyond f_d. A gyrokinetic equation for F needs to be derived, whose solution will be used to calculate the viscous stress tensor $\mathbf{\Pi}(\mathbf{x},t)$ and the heat stress tensor $\mathbf{\Theta}(\mathbf{x},t)$ such that the fluid equations for $n(\mathbf{x},t)$, $T(\mathbf{x},t)$, $\mathbf{V}(\mathbf{x},t)$, and $\mathbf{q}(\mathbf{x},t)$ can be closed. F is also needed to calculate the charge density and the current density in Maxwell's equations. Besides tokamak plasmas, the gyrokinetic system for general equilibria may have applications in other branches of plasma physics. For example, we notice the similarity between the particles' trajectories in a cylindrical neutral plasma with flow in the $\mathbf{e}_\theta$ direction and a cylindrical nonneutral plasma confined radially by a magnetic field in the $\mathbf{e}_z$ direction.[69] In both cases, the particles' trajectories are circular orbits in the $\mathbf{e}_\theta$ direction, on top of which the fast time scale gyromotions are added. For space plasmas, hybrid, perturbative kinetic MHD is not applicable to many interesting problems. One example is collisionless reconnection, which is thought to be relevant to magnetic storms in the magnetosphere. Recent magnetic reconnection experiments at the Princeton Plasma Physics Laboratory suggested that ''anomalous resistivity'' could be the key to understanding magnetic reconnection phenomena.[70] A fully kinetic model is necessary to explain the observed ''anomalous resistivity,'' which is much bigger than the classical resistivity due to Coulomb collisions. Another example is the mechanism of parallel acceleration for charged particles near the magnetic poles of the earth, which explains the aurora phenomena. Perturbative kinetic MHD cannot describe the parallel acceleration, because the ideal MHD Ohm's law adopted implies $E_\parallel=0$. Also, strong wave-particle interaction is expected to be important for the parallel acceleration of charged particles.

ACKNOWLEDGMENTS

This work is supported by U.S. Department of Energy Contract No. DE-AC02-76-CH0-3073. We thank Professor L. Chen, Dr. W. W. Lee, Dr. T. S. Hahm, Dr. Z. H. Lin, Dr. G. Y. Fu, and Dr. J. Manickam for constructive comments and suggestions.

APPENDIX A: ORBIT INTEGRAL FOR DISTRIBUTION FUNCTION

The result of orbit integration for h and relevant definitions are as follows. Detailed calculations can be found in Ref. 40:

$$h=-i\frac{e}{T}F_0\sum_m e^{-im\theta}[\omega-\omega_*^T(r)]J_0\sum_n\left\{\left[a_n\phi_m(r)-\left(a_n-a_n^G\frac{\overline{\omega}_D(r)}{\omega}\right)\psi_{\|m}(r)\right]D(n)+\left[a_n\phi_m'(r)-\left(a_n-a_n^G\frac{\overline{\omega}_D(r)}{\omega}\right)\psi_{\|m}'(r)\right]\sum_{n_1} r_{n_1}e^{in_1\omega_b\hat{t}}[D(n+n_1)-D(n)]+\left[a_n\phi_m''(r)-\left(a_n-a_n^G\frac{\overline{\omega}_D(r)}{\omega}\right)\times\psi_{\|m}''(r)\right]\frac{1}{2}\sum_{n_1,n_2} r_{n_1}r_{n_2}e^{i(n_1+n_2)\omega_b\hat{t}}[D(n+n_1+n_2)-D(n+n_1)-D(n+n_2)+D(n)]\right\}, \tag{A1}$$

where we have defined

$$D(n)\equiv\frac{1}{\omega-\omega_D^{(0)}-(n+H\sigma_\|S)\omega_{b,t}}, \tag{A2}$$

$$r_n\equiv\begin{cases}\dfrac{\rho_\theta\sqrt{Y}\sqrt{\epsilon}I_n}{\pi L_b}, & \text{odd } n,\\ 0, & \text{even } n,\end{cases} \tag{A3}$$

$$a_n\equiv\begin{cases}e^{-i[nS\theta-n\omega_b\hat{t}]}\dfrac{\sqrt{\epsilon}}{\pi L_b}J_{n,m}, & \text{trapped},\\ e^{-i[nS\theta-(n+\sigma_\|S)\omega_t\hat{t}]}\dfrac{\sqrt{\epsilon}}{\pi L_t}K_{n,m,m}, & \text{circulating},\end{cases} \tag{A4}$$

$$a_n^G\equiv\begin{cases}e^{-i[nS\theta-n\omega_b\hat{t}]}\dfrac{\sqrt{\epsilon}}{\pi L_b}J_{n,m}^G, & \text{trapped},\\ e^{-i[nS\theta-(n+\sigma_\|S)\omega_t\hat{t}]}\dfrac{\sqrt{\epsilon}}{\pi L_t}K_{n,m,m}^G, & \text{circulating},\end{cases}$$

$$\hat{t}(\theta,\sigma_\|)\equiv\begin{cases}\dfrac{R_0q}{\sqrt{Y}v_{th}}\displaystyle\int_0^\theta\frac{d\theta}{\sqrt{1-\Lambda/\alpha(\theta)}}, & \text{trapped, } \sigma_\|=1,\\ \dfrac{\tau_b}{2}-\hat{t}(\theta,\sigma_\|=1), & \text{trapped, } \sigma_\|=-1,\\ \dfrac{R_0q\sigma_\|}{\sqrt{Y}v_{th}}\displaystyle\int_0^\theta\frac{d\theta}{\sqrt{1-\Lambda/\alpha(\theta)}}, & \text{circulating},\end{cases} \tag{A5}$$

$$I_n\equiv\int_0^{\theta_0}d\theta\cos(n\omega_b\hat{t}), \tag{A6}$$

$$J_{n,m}\equiv\int_0^{\theta_0}d\theta\left[\cos^2\frac{n\pi}{2}\cos S\theta\cos n\omega_b\hat{t}+\sin^2\frac{n\pi}{2}\sin S\theta\sin n\omega_b\hat{t}\right],$$

$$J_{n,m}^G\equiv\int_0^{\theta_0}d\theta G(\theta)\left[\cos^2\frac{n\pi}{2}\cos S\theta\cos n\omega_b\hat{t}+\sin^2\frac{n\pi}{2}\sin S\theta\sin n\omega_b\hat{t}\right], \tag{A7}$$

$$K_{n,p,m}\equiv\int_0^\pi\frac{d\theta}{\sqrt{1-\Lambda/\alpha(\theta)}}\cos[S\theta-(n+\sigma_\|S)\omega_t\hat{t}],$$

$$K_{n,p,m}^G\equiv\int_0^\pi\frac{d\theta}{\sqrt{1-\Lambda/\alpha(\theta)}}G(\theta)\cos[S\theta-(n+\sigma_\|S)\omega_t\hat{t}], \tag{A8}$$

$$L_b\equiv\frac{\sqrt{\epsilon}}{\pi}\int_0^{\theta_0}d\theta\frac{d\theta}{\sqrt{1-\Lambda/\alpha(\theta)}},$$

$$L_t\equiv\frac{\sqrt{\epsilon}}{\pi}\int_0^{\pi}d\theta\frac{d\theta}{\sqrt{1-\Lambda/\alpha(\theta)}}, \tag{A9}$$

$$\omega_D\equiv n\left[\frac{d\zeta}{dt}-q(r^0)\frac{d\theta}{dt}\right],$$

$$\omega_D^{(0)}\equiv\frac{1}{\tau_{t,b}}\oint\omega_D\,dt, \tag{A10}$$

$$\Delta\omega_D\equiv\omega_D-\omega_D^{(0)},$$

$$S=S(r^0)\equiv nq(r^0)-m,\quad r^0\equiv\frac{1}{\tau_{t,b}}\oint r\,dt, \tag{A11}$$

$$\tau_b \equiv \frac{4R_0 q}{\sqrt{Y} v_{th}} \int_0^{\theta_0} \frac{d\theta}{\sqrt{1-\Lambda/\alpha(\theta)}},$$

$$\tau_t \equiv \frac{2R_0 q}{\sqrt{Y} v_{th}} \int_0^{\pi} \frac{d\theta}{\sqrt{1-\Lambda/\alpha(\theta)}}, \tag{A12}$$

$$\omega_{b,t} \equiv \frac{2\pi}{\tau_{b,t}},$$

$$G(\theta) = \left(1 + \frac{U^2}{v^2}\right)\cos(\theta) + 2\frac{\hat{s}}{\epsilon}\frac{(U-U^{(0)})U}{v^2},$$

and

$$\theta_0 \equiv \cos^{-1}\left[\frac{\Lambda-1}{\epsilon}\right], \quad Y \equiv \frac{\epsilon}{T}, \quad \Lambda \equiv \frac{\mu B}{\epsilon},$$

$$\rho_\theta \equiv v_{th}\frac{cm}{eB_\theta}, \quad \hat{s} \equiv \frac{r}{q}\frac{dq}{dr}. \tag{A13}$$

Here, μ is the magnetic moment; ϵ is the kinetic energy; $\sigma_\parallel = 1$ for positive U; and $\sigma_\parallel = -1$ for negative U. All other symbols have their usual meaning.

The following approximations for ω_D and $U^{(0)}$ will be adopted:[71]

$$\omega_D = \bar{\omega}_D \frac{\epsilon}{T} G(\theta), \tag{A14}$$

with

$$\bar{\omega}_D = \omega_*^{(m)} \frac{L_n}{R_0}\frac{nq}{m}, \quad \omega_*^{(m)} = \frac{cTm}{L_n eBr}, \quad L_n = -\left(\frac{d\ln n_0}{dx}\right)^{-1}, \tag{A15}$$

and

$$U^{(0)} = \begin{cases} 0, & \text{trapped,} \\ U, & \text{circulating.} \end{cases} \tag{A16}$$

APPENDIX B: EXPRESSIONS FOR MATRICES *A*, *B*, AND *C*

The matrix elements involving the distribution function can be simplified using the methods described by Marchand *et al.*[41] Other matrix elements are easily obtained by applying the GVA computer algebra program. Detailed calculations are carried out in Ref. 40. Here we only list the final results:

$$\begin{pmatrix} A_{pm}^{QN\phi} & A_{pm}^{QN\psi} \\ A_{pm}^{F\phi} & A_{pm}^{F\psi} \end{pmatrix} = \sum_j \frac{n_j}{n_e} Z_j^2 \frac{T_e}{T_j} \frac{\epsilon^{3/2}\rho_{\theta j}^2}{2\pi^{9/2}} \int_{1-\epsilon}^{1+\epsilon} d\Lambda \frac{1}{L_b^3} \int_0^\infty dY Y^{3/2} e^{-Y} \sum_n \frac{\omega - \omega_{*j}^T}{\omega - \omega_D^{(0)} - n\omega_{b,j}} \sum_{n_1, n2\,\mathrm{odd}} I_{n_1} I_{n_2}$$

$$\times \begin{pmatrix} J_{n,m}J_{n+n_1+n_2,p} - 2J_{n-n_2,m}J_{n+n_1,p} & -\left(J_{n,m} - \frac{\bar{\omega}_{dj}}{\omega} Y J_{n,m}^G\right) J_{n+n_1+n_2,p} \\ + J_{n-n_1-n_2,m}J_{n,p} & +2\left(J_{n-n_2,m} - \frac{\bar{\omega}_{dj}}{\omega} Y J_{n-n_2,m}^G\right) J_{n+n_1,p} \\ & -\left(J_{n-n_1-n_2,m} - \frac{\bar{\omega}_{dj}}{\omega} Y J_{n-n_1-n_2,m}^G\right) J_{n,p} \\ -\left(\frac{rR_0\omega}{\lambda_e c}\right)^2 \frac{\bar{\omega}_{dj}}{\omega} Y [J_{n,m}J_{n+n_1+n_2,p}^G & -\left(\frac{rR_0\omega}{\lambda_e c}\right)^2 \frac{\bar{\omega}_{dj}}{\omega} Y \left[-\left(J_{n,m} - \frac{\bar{\omega}_{dj}}{\omega} Y J_{n,m}^G\right) J_{n+n_1+n_2,p}^G \right. \\ -2J_{n-n_2,m}J_{n+n_1,p}^G + J_{n-n_1-n_2,m}J_{n,p}^G] & +2\left(J_{n-n_2,m} - \frac{\bar{\omega}_{dj}}{\omega} Y J_{n-n_2,m}^G\right) J_{n+n_1,p}^G \\ & \left. -\left(J_{n-n_1-n_2,m} - \frac{\bar{\omega}_{dj}}{\omega} Y J_{n-n_1-n_2,m}^G\right) J_{n,p}^G \right] \end{pmatrix}, \tag{B1}$$

where $\lambda_e \equiv T_e/(4\pi n_e e^2)$ is the electron Debye length.

$$\begin{pmatrix} B_{pm}^{QN\phi} & B_{pm}^{QN\psi} \\ B_{pm}^{F\phi} & B_{pm}^{F\psi} \end{pmatrix}$$

$$= \sum_j \frac{n_j}{n_e} Z_j^2 \frac{T_e}{T_j} \frac{\epsilon\rho_{\theta j}}{\pi^{7/2}} \int_{1-\epsilon}^{1+\epsilon} d\Lambda \frac{1}{L_b^2} \int_0^\infty dY Y e^{-Y} \sum_n \frac{\omega - \omega_{*j}^T}{\omega - \omega_D^{(0)} - n\omega_{b,j}} \sum_{n_1\,\mathrm{odd}} I_{n_1}$$

$$\times\begin{pmatrix} J_{n-n_1,m}J_{n,p}-J_{n,m}J_{n+n_1,p} & -\left(J_{n-n_1,m}-\frac{\overline{\omega}_{dj}}{\omega}YJ^G_{n-n_1,m}\right)J_{n,p} \\ & +\left(J_{n,m}-\frac{\overline{\omega}_{dj}}{\omega}YJ^G_{n,m}\right)J_{n+n_1,p} \\ -\left(\frac{rR_0\omega}{\lambda_e c}\right)^2(J_{n-n_1,m}J^G_{n,p}-J_{n,m}J^G_{n+n_1,p}) & -\left(\frac{rR_0\omega}{\lambda_e c}\right)^2\Bigg[-\left(J_{n-n_1,m}-\frac{\overline{\omega}_{dj}}{\omega}YJ^G_{n-n_1,m}\right)J^G_{n,p} \\ & +\left(J_{n,m}-\frac{\overline{\omega}_{dj}}{\omega}YJ^G_{n,m}\right)J^G_{n+n_1,p}\Bigg] \end{pmatrix}+\begin{pmatrix}0&0\\0&B^P_{pm}\end{pmatrix}. \tag{B2}$$

We have neglected the contribution of circulating particles to the A and B matrices, because the radial excursions of the circulating particles are much smaller than those of the trapped particles.

$$\begin{aligned}\begin{pmatrix} C^{QN\phi}_{pm} & C^{QN\psi}_{pm} \\ C^{F\phi}_{pm} & C^{F\psi}_{pm}\end{pmatrix} &= \sum_j \frac{n_j}{n_e}Z_j^2\frac{T_e}{T_j}\frac{\sqrt{\epsilon}}{\pi^{5/2}}\int_{1-\epsilon}^{1+\epsilon}d\Lambda\frac{1}{L_b}\int_0^\infty dY\sqrt{Y}e^{-Y}\sum_n\frac{\omega-\omega^T_{*j}}{\omega-\omega^{(0)}_D-n\omega_{b,j}} \\ &\times\begin{pmatrix} J_{n,p}J_{n,m} & -J_{n,p}\left(J_{n,m}-\frac{\overline{\omega}_{dj}}{\omega}YJ^G_{n,m}\right) \\ -\left(\frac{rR_0\omega}{\lambda_e c}\right)^2\frac{\overline{\omega}_{dj}}{\omega}YJ^G_{n,p}J_{n,m} & \left(\frac{rR_0\omega}{\lambda_e c}\right)^2\frac{\overline{\omega}_{dj}}{\omega}YJ^G_{n,p}\left(J_{n,m}-\frac{\overline{\omega}_{dj}}{\omega}YJ^G_{n,m}\right)\end{pmatrix} \\ &+\sum_j\frac{n_j}{n_e}Z_j^2\frac{T_e}{T_j}\frac{\sqrt{\epsilon}}{\pi^{5/2}}\int_0^{1-\epsilon}d\Lambda\frac{1}{L_t}\int_0^\infty dY\sqrt{Y}e^{-Y}\sum_n\frac{(\omega-\omega^T_{*j})\omega}{\omega^2-(n+S)^2\omega^2_{t,j}} \\ &\times\begin{pmatrix} K_{n,p,m}K_{n,m,m} & -K_{n,p,m}\left(K_{n,m,m}-\frac{\overline{\omega}_{dj}}{\omega}YK^G_{n,m,m}\right) \\ -\left(\frac{rR_0\omega}{\lambda_e c}\right)^2\frac{\overline{\omega}_{dj}}{\omega}YK^G_{n,p,m}K_{n,m,m} & \left(\frac{rR_0\omega}{\lambda_e c}\right)^2\frac{\overline{\omega}_{dj}}{\omega}YK^G_{n,p,m}\left(K_{n,m,m}-\frac{\overline{\omega}_{dj}}{\omega}YK^G_{n,m,m}\right)\end{pmatrix} \\ &+\sum_j\frac{n_j}{n_e}Z_j^2\frac{T_e}{T_j}\begin{pmatrix} -\delta_{p,m} & \delta_{p,m}e^{-b_j}\left\{I_0-\frac{\omega_{*j}}{\omega}[I_0+\eta_j b_j(I_0-I_1)]\right\} \\ 0 & 0\end{pmatrix}+\begin{pmatrix}0&0\\0&C^P_{pm}\end{pmatrix},\end{aligned} \tag{B3}$$

$$\begin{aligned}A^{J\phi}_{pm} &= x^2(\delta_{p,m}O_2^{\phi''}+\epsilon\delta_{p+1,m}U_1^{\phi''}+\epsilon\delta_{p-1,m}D_1^{\phi''} \\ &\quad+\epsilon^2\delta_{p+2,m}U_2^{\phi''}+\epsilon^2\delta_{p-2,m}D_2^{\phi''}+\epsilon^2\delta_{p,m}S^{\phi''}),\\ A^{J\psi}_{pm} &= x^2(\delta_{p,m}O_2^{\psi''}+\epsilon\delta_{p+1,m}U_1^{\psi''}+\epsilon\delta_{p-1,m}D_1^{\psi''} \\ &\quad+\epsilon^2\delta_{p+2,m}U_2^{\psi''}+\epsilon^2\delta_{p-2,m}D_2^{\psi''}+\epsilon^2\delta_{p,m}S^{\psi''});\end{aligned} \tag{B4}$$

$$\begin{aligned}B^{J\phi}_{pm} &= x^2(\delta_{p,m}O_2^{\phi'}+\epsilon\delta_{p+1,m}U_1^{\phi'}+\epsilon\delta_{p-1,m}D_1^{\phi'} \\ &\quad+\epsilon^2\delta_{p+2,m}U_2^{\phi'}+\epsilon^2\delta_{p-2,m}D_2^{\phi''}+\epsilon^2\delta_{p,m}S^{\phi'}),\\ B^{J\psi}_{pm} &= x^2(\delta_{p,m}O_2^{\psi'}+\epsilon\delta_{p+1,m}U_1^{\psi'}+\epsilon\delta_{p-1,m}D_1^{\psi'} \\ &\quad+\epsilon^2\delta_{p+2,m}U_2^{\psi'}+\epsilon^2\delta_{p-2,m}D_2^{\psi'}+\epsilon^2\delta_{p,m}S^{\psi'});\end{aligned} \tag{B5}$$

$$\begin{aligned}C^{J\phi}_{pm} &= x^2(\delta_{p,m}O_2^{\phi}+\epsilon\delta_{p+1,m}U_1^{\phi}+\epsilon\delta_{p-1,m}D_1^{\phi} \\ &\quad+\epsilon^2\delta_{p+2,m}U_2^{\phi}+\epsilon^2\delta_{p-2,m}D_2^{\phi}+\epsilon^2\delta_{p,m}S^{\phi}),\\ C^{J\psi}_{pm} &= x^2(\delta_{p,m}O_2^{\psi}+\epsilon\delta_{p+1,m}U_1^{\psi}+\epsilon\delta_{p-1,m}D_1^{\psi} \\ &\quad+\epsilon^2\delta_{p+2,m}U_2^{\psi}+\epsilon^2\delta_{p-2,m}D_2^{\psi}+\epsilon^2\delta_{p,m}S^{\psi});\\ B^P_{pm} &= x^2[\epsilon\delta_{p-1,m}(-\overline{P}'m)+\epsilon\delta_{p+1,m}(\overline{P}'m) \\ &\quad+\epsilon^2\delta_{p-2,m}(-\overline{P}'\tfrac{1}{2}m)+\epsilon^2\delta_{p+2,m}(\overline{P}'\tfrac{1}{2}m)],\end{aligned} \tag{B6}$$

$$C_{pm}^{P}=x^2\Big\{\epsilon\delta_{p-1,m}[\overline{P}'(m-m^2)-\overline{P}''mx]+\epsilon\delta_{p+1,m}[\overline{P}'(-m-m^2)+\overline{P}''mx]+\epsilon^2\delta_{p-2,m}[\overline{P}'\tfrac{1}{2}(m-m^2)-\overline{P}''\tfrac{1}{2}mx]+\epsilon^2\delta_{p+2,m}[\overline{P}'\tfrac{1}{2}(-m-m^2)+\overline{P}''\tfrac{1}{2}mx]+\epsilon^2\delta_{p,m}\left[-\overline{P}'m^2-\overline{P}'m^2\frac{q'x}{q^3}\right]\Big\}; \tag{B7}$$

$$\overline{P}'=\frac{4\pi R_0^2}{a^2B_0^2}\frac{dP}{dx},\qquad \overline{P}''=\frac{4\pi R_0^2}{a^2B_0^2}\frac{d^2P}{dx^2}. \tag{B8}$$

In the above equations, the independent variable in the radial direction is $x\equiv r/a$, the normalized r. The expressions for O_2, U_1, D_1, U_2, D_2, and S are calculated by the method of computer algebra, and can be found in Ref. 39, 40, and 48.

[1] M. N. Rosenbluth and M. L. Sloan, Phys. Fluids **14**, 1725 (1971).
[2] W. M. Tang, Nucl. Fusion **18**, 1089 (1978).
[3] J. Q. Dong, P. N. Guzdar, and Y. C. Lee, Phys. Fluids **30**, 2694 (1987).
[4] G. Rewoldt, W. M. Tang, and M. S. Chance, Phys. Fluids **25**, 480 (1982).
[5] M. Kotschenreuther, G. Rewoldt, and W. M. Tang, Comput. Phys. Commun. **88**, 128 (1995).
[6] K. McGuire, R. Goldston, and M. Bell, *et al.*, Phys. Rev. Lett. **50**, 891 (1983).
[7] L. Chen, R. B. White, and M. N. Rosenbluth, Phys. Rev. Lett. **52**, 1122 (1984).
[8] C. Z. Cheng and M. S. Chance, Phys. Fluids **29**, 3695 (1986).
[9] G. Y. Fu and J. W. Van Dam, Phys. Fluids B **1**, 1949 (1989).
[10] C. Z. Cheng, Phys. Rep. **211**, 1 (1992).
[11] C. Z. Cheng, H. L. Berk, D. Borba, *et al.*, *Proceeding of the 11th International Conference on Plasma Physics and Controlled Nuclear Fusion Research*, Montreal, 1996 (International Atomic Energy Agency, Vienna, 1997), **2**, 953.
[12] W. M. Tang, J. W. Connor, and R. J. Hastie, Nucl. Fusion **21**, 1439 (1980).
[13] E. A. Frieman, G. Rewoldt, W. M. Tang, and A. H. Glasser, Phys. Fluids **23**, 1750 (1980).
[14] J. Jacquinot and the JET team, *Proceeding of the 11th International Conference on Plasma Physics and Controlled Nuclear Fusion Research* Kyoto, 1986 (International Atomic Energy Agency, Vienna, 1987), **1**, 449.
[15] R. B. White, M. N. Bussac, and F. Romanelli, Phys. Rev. Lett. **62**, 539 (1989).
[16] R. B. White, *Theory of Tokamak Plasmas* (North-Holland, Amsterdam, 1989), pp. 248–283.
[17] H. L. Berk, J. W. Van Dam, Z. Guo, and D. M. Lindberg, Phys. Fluids B **4**, 1806 (1992).
[18] G. Y. Fu, C. Z. Cheng, and K. L. Wong, Phys. Fluids B **5**, 4040 (1993).
[19] G. Y. Fu, private communication (1998).
[20] C. Z. Cheng, private communication (1998).
[21] P. J. Catto, W. M. Tang, and D. E. Baldwin, Plasma Phys. **23**, 639 (1981).
[22] T. M. Antonsen and B. Lane, Phys. Fluids **23**, 1205 (1980).
[23] H. Qin, W. M. Tang, W. W. Lee, and G. Rewoldt, Phys. Plasmas **6**, 1575 (1999).
[24] G. Rewoldt, W. M. Tang, and R. J. Hastie, Phys. Fluids **30**, 807 (1987).
[25] R. J. Hastie, J. B. Taylor, and F. A. Haas, Ann. Phys. **41**, 302 (1967).
[26] P. H. Rutherford and E. A. Frieman, Phys. Fluids **11**, 569 (1968).
[27] E. A. Frieman and L. Chen, Phys. Fluids **25**, 502 (1982).
[28] W. W. Lee, Phys. Fluids **26**, 556 (1983).
[29] D. H. E. Dubin, J. A. Krommes, C. Oberman, and W. W. Lee, Phys. Fluids **26**, 3524 (1983).
[30] R. G. Littlejohn, Phys. Fluids **27**, 976 (1984).
[31] T. S. Hahm, W. W. Lee, and A. Brizard, Phys. Fluids **31**, 1940 (1988).
[32] T. S. Hahm, Phys. Fluids **31**, 2670 (1988).
[33] A. J. Brizard, J. Plasma Phys. **41**, 541 (1989).
[34] A. J. Brizard, Phys. Fluids B **1**, 1381 (1989).
[35] A. J. Brizard, Ph. D. Dissertation (Princeton University, 1990).
[36] V. D. Shafranov, Sov. Phys. Tech. Phys. **15**, 175 (1970).
[37] M. N. Rosenbluth, R. Y. Dagazian, and P. H. Rutherford, Phys. Fluids **16**, 1894 (1973).
[38] M. N. Bussac, R. Pellat, D. Edery, and J. L. Soule, Phys. Rev. Lett. **35**, 1638 (1975).
[39] H. Qin, W. M. Tang, and G. Rewoldt, Phys. Plasmas **5**, 1035 (1998).
[40] H. Qin, Ph. D. Dissertation (Princeton University, 1998).
[41] R. Marchand, Ph.D. Dissertation (Princeton University, 1979).
[42] R. Marchand, W. M. Tang, and G. Rewoldt, Phys. Fluids **23**, 1164 (1980).
[43] W. M. Tang and G. Rewoldt, Phys. Fluids B **5**, 2451 (1993).
[44] J. Manickam, Nucl. Fusion **24**, 595 (1984).
[45] M. Artun, Ph. D. Dissertation, Princeton University (1994).
[46] M. Artun, W. M. Tang, and G. Rewoldt, Phys. Plasmas **2**, 3384 (1995).
[47] G. Rewoldt, unpublished notes.
[48] H. Qin, W. M. Tang, and G. Rewoldt, Comput. Phys. Commun. **16**, 107 (1999).
[49] D. Dorbrott, D. B. Nelson, J. M. Green, A. H. Glasser, M. S. Chance, and E. A. Frieman, Phys. Rev. Lett. **39**, 943 (1977).
[50] B. Coppi, Phys. Rev. Lett. **39**, 939 (1977).
[51] W. M. Tang, G. Rewoldt, C. Z. Cheng, and M. S. Chance, Nucl. Fusion **25**, 152 (1985).
[52] J. W. Connor, R. J. Hastie, and J. W. Taylor, Phys. Rev. Lett. **40**, 396 (1978).
[53] J. P. Freidberg, *op. cit.*, pp. 338–342.
[54] Y. P. Pao, Phys. Fluids **19**, 1796 (1976).
[55] R. M. O. Galvao, P. H. Sakanaka, and H. Shigueoka, Phys. Rev. Lett. **41**, 870 (1978).
[56] W. Kerner, R. Gruber, and F. Troyon, Phys. Rev. Lett. **44**, 536 (1980).
[57] H. R. Strauss, Phys. Fluids **19**, 134 (1976).
[58] H. R. Strauss, Phys. Fluids **20**, 1354 (1977).
[59] H. Naitou, K. Tsuda, W. W. Lee, and R. D. Sydora, Phys. Plasmas **2**, 4257 (1995).
[60] R. D. Hazeltine and J. D. Meiss, *Plasma Confinement* (Addison-Wesley, Reading, MA 1992), p. 267.
[61] J. Manickam, private communication (1998).
[62] K. L. Wong, R. Fonck, S. Paul, *et al.*, Phys. Rev. Lett. **66**, 1874 (1991).
[63] R. Nazikian, G. Y. Fu, Z. Chang, *et al.*, Phys. Plasmas **5**, 1703 (1998).
[64] A. J. Brizard, Phys. Plasmas **2**, 459 (1995).
[65] T. S. Hahm, Phys. Plasmas **3**, 4658 (1996).
[66] J. D. Callen, private communication, plasma theory seminar, Princeton Plasma Physics Laboratory (1998).
[67] J. D. Callen, private communication (1998).
[68] T. S. Hahm, private communication, (1998).
[69] R. C. Davidson, *Physics of Nonneutral Plasmas* (Addison-Wesley, Reading, MA 1990), pp. 47–52.
[70] H. Ji, M. Yamada, S. Hsu, and R. Kulsrud, Phys. Rev. Lett. **80**, 3256 (1998).
[71] B. Coppi and G. Rewoldt, in *Advances in Plasma Physics*, Vol. 6 (Wiley, New York, 1976), p. 523.